



# Characterizing a World Within the Hot-Neptune Desert: Transit Observations of LTT 9779 b with the Hubble Space Telescope/WFC3

Billy Edwards<sup>1,9</sup> , Quentin Changeat<sup>2</sup> , Angelos Tsiaras<sup>3</sup> , Andrew Allan<sup>4</sup>, Patrick Behr<sup>5</sup> , Simone R. Hagey<sup>6</sup> , Michael D. Himes<sup>7,8</sup> , Sushuang Ma<sup>9</sup> , Keivan G. Stassun<sup>10</sup> , Luis Thomas<sup>9,11,12</sup>, Alexandra Thompson<sup>9</sup> , Aaron Boley<sup>6</sup> , Luke Booth<sup>13</sup>, Jeroen Bouwman<sup>14</sup>, Kevin France<sup>5</sup> , Nataliea Lawson<sup>15</sup> , Annabella Meech<sup>16</sup> , Caprice L. Phillips<sup>17</sup> , Aline A. Vidotto<sup>4</sup> , Kai Hou Yip<sup>9</sup> , Michelle Bieger<sup>18</sup> , Amélie Gressier<sup>19</sup> , Estelle Janin<sup>20</sup>, Ing-Guey Jiang<sup>21</sup> , Pietro Leonardi<sup>22,23</sup> , Subhajit Sarkar<sup>13</sup>, Nour Skaf<sup>9,24,25</sup> , Jake Taylor<sup>26,27</sup> , Ming Yang<sup>28</sup> , and Derek Ward-Thompson<sup>29</sup> 

<sup>1</sup>SRON, Netherlands Institute for Space Research, Niels Bohrweg 4, NL-2333 CA, Leiden, The Netherlands; [b.edwards@sron.nl](mailto:b.edwards@sron.nl)

<sup>2</sup>European Space Agency (ESA), ESA Office, Space Telescope Science Institute (STScI), Baltimore, MD 21218, USA

<sup>3</sup>INAF, Osservatorio Astrofisico di Arcetri, Largo E. Fermi 5, I-50125 Firenze, Italy

<sup>4</sup>Leiden Observatory, Leiden University, PO Box 9513, 2300 RA Leiden, The Netherlands

<sup>5</sup>Laboratory for Atmospheric and Space Physics, University of Colorado Boulder, Boulder, CO 80303, USA

<sup>6</sup>The University of British Columbia, 6224 Agricultural Road, Vancouver, BC V6T 1Z1, Canada

<sup>7</sup>Planetary Sciences Group, Department of Physics, University of Central Florida, Orlando, FL, USA

<sup>8</sup>NASA Postdoctoral Program Fellow, NASA Goddard Space Flight Center, Greenbelt, MD, USA

<sup>9</sup>Department of Physics and Astronomy, University College London, Gower Street, London WC1E 6BT, UK

<sup>10</sup>Department of Physics and Astronomy, Vanderbilt University, Nashville, TN 37235, USA

<sup>11</sup>Universitäts-Sternwarte München, Scheinerstr. 1, D-81679 München, Germany

<sup>12</sup>Max-Planck-Institut für extraterrestrische Physik, Giessenbachstrasse 1, D-85748 Garching, Germany

<sup>13</sup>Cardiff Hub for Astrophysics Research and Technology (CHART), School of Physics and Astronomy, Cardiff University, Cardiff, UK

<sup>14</sup>Max-Planck-Institut für Astronomie, Königstuhl 17, D-69117 Heidelberg, Germany

<sup>15</sup>Centre for Astrophysics, University of Southern Queensland, 499-565 West Street, Toowoomba, QLD 4350, Australia

<sup>16</sup>Department of Physics, University of Oxford, Denys Wilkinson Building, Oxford OX1 3RH, UK

<sup>17</sup>Department of Astronomy, The Ohio State University, 100 W 18th Ave, Columbus, OH 43210, USA

<sup>18</sup>College of Engineering, Mathematics and Physical Sciences, University of Exeter, North Park Road, Exeter, UK

<sup>19</sup>Space Telescope Science Institute, 3700 San Martin Drive, Baltimore, MD 21218, USA

<sup>20</sup>Arizona State University, P.O. Box 871404, Tempe, AZ 85287-1404, USA

<sup>21</sup>Department of Physics and Institute of Astronomy, National Tsing Hua University, Hsinchu 30013, Taiwan

<sup>22</sup>Dipartimento di Fisica, Università di Trento, Via Sommarive 14, I-38123 Povo, Italy

<sup>23</sup>Dipartimento di Fisica e Astronomia, Università degli Studi di Padova, Vicolo dell'Osservatorio 3, I-35122 Padova, Italy

<sup>24</sup>LESIA, Observatoire de Paris, Univ. Paris Cité, Univ. PSL, CNRS, Sorbonne Univ., 5 pl. Jules Janssen, F-92195 Meudon, France

<sup>25</sup>National Astronomical Observatory of Japan, Subaru Telescope, 650 North A'ohōkū Place, Hilo, HI 96720, USA

<sup>26</sup>Department of Physics (Atmospheric, Oceanic and Planetary Physics), University of Oxford, Parks Road, Oxford OX1 3PU, UK

<sup>27</sup>Institut Trotter de Recherche sur les Exoplanètes et Département de Physique, Université de Montréal, 1375 Avenue Thérèse-Lavoie-Roux, Montréal, QC H2V 0B3, Canada

<sup>28</sup>College of Surveying and Geo-Informatics, Tongji University, Shanghai 200092, People's Republic of China

<sup>29</sup>Jeremiah Horrocks Institute, University of Central Lancashire, Preston PR1 2HE, UK

Received 2023 April 30; revised 2023 June 21; accepted 2023 June 21; published 2023 September 15

## Abstract

We present an atmospheric analysis of LTT 9779 b, a rare planet situated in the hot-Neptune desert, that has been observed with Hubble Space Telescope (HST)/WFC3 with G102 and G141. The combined transmission spectrum, which covers 0.8–1.6  $\mu\text{m}$ , shows a gradual increase in transit depth with wavelength. Our preferred atmospheric model shows evidence for H<sub>2</sub>O, CO<sub>2</sub>, and FeH with a significance of 3.1 $\sigma$ , 2.4 $\sigma$ , and 2.1 $\sigma$ , respectively. In an attempt to constrain the rate of atmospheric escape for this planet, we search for the 1.083  $\mu\text{m}$  helium line in the G102 data but find no evidence of excess absorption that would indicate an escaping atmosphere using this tracer. We refine the orbital ephemerides of LTT 9779 b using our HST data and observations from TESS, searching for evidence of orbital decay or apsidal precession, which are not found. The phase-curve observation of LTT 9779 b with JWST NIRISS should provide deeper insights into the atmosphere of this planet and the expected atmospheric escape might be detected with further observations concentrated on other tracers such as Ly $\alpha$ .

*Unified Astronomy Thesaurus concepts:* Exoplanets (498); Hot Neptunes (754); Infrared spectroscopy (2285); Hubble Space Telescope (761)

## 1. Introduction

The exoplanet field has rapidly expanded, with thousands of planets currently known and thousands more anticipated in the coming decade, thanks to dedicated planet-hunting missions

such as Kepler (Borucki et al. 2010) and the Transiting Exoplanet Survey Satellite (TESS; Ricker et al. 2014). The vast number of detected worlds enables characterization of a diverse exoplanet sample to be further characterized, with low-resolution space-based spectroscopy detecting broadband spectral features of molecular species in exoplanet atmospheres (e.g., Tinetti et al. 2007; Swain et al. 2008).

For over a decade, the Hubble Space Telescope (HST) has been utilized to conduct observations of the atmospheres of



Original content from this work may be used under the terms of the [Creative Commons Attribution 4.0 licence](https://creativecommons.org/licenses/by/4.0/). Any further distribution of this work must maintain attribution to the author(s) and the title of the work, journal citation and DOI.

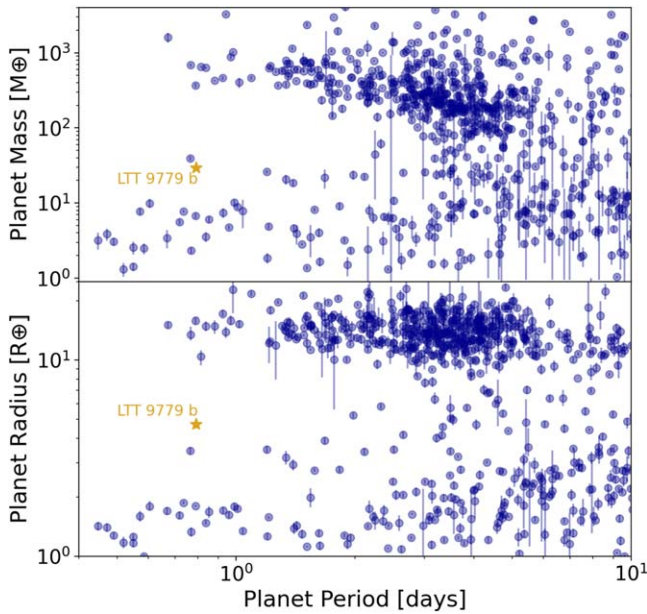


**Figure 1.** LTT 9779 b in context with the known population of transiting planets. In the period–mass and period–radius spaces, LTT 9779 b occupies a region which is sparsely populated. The majority of other planets on such a short orbital period are either stripped rocky cores or Jupiter-sized worlds.

exoplanets. With the spatial scanning technique allowing for higher signal-to-noise ratio (S/N) observations (McCullough & MacKenty 2012), the characterization of exoplanetary atmospheres via the transit (e.g., Kreidberg et al. 2014; Luque et al. 2020; Murgas et al. 2020; Skaf et al. 2020; Wilson et al. 2020; Yan et al. 2020; Guilluy et al. 2021; Yip et al. 2021; McGruder et al. 2022; Saba et al. 2022), eclipse (e.g., Line et al. 2016; Edwards et al. 2020b; Pluriel et al. 2020; Changeat & Edwards 2021; Jacobs et al. 2022), and phase-curve (e.g., Stevenson et al. 2014, 2017; Kreidberg et al. 2018; Arcangeli et al. 2019; Changeat et al. 2021; Changeat 2022; Robbins-Blanch et al. 2022) techniques has rapidly expanded. Indeed, enough planets have now been studied to facilitate population-style studies (e.g., Sing et al. 2016; Fisher & Heng 2018; Tsiaras et al. 2018; Cubillos & Blecic 2021; Mansfield et al. 2021; Roudier et al. 2021; Changeat et al. 2022; Edwards et al. 2022).

Numerous short-period planets have been discovered and these usually fall into one of two populations: large, gaseous worlds (i.e., hot Jupiters) or stripped rocky cores which are often referred to as ultrashort-period planets. Between these two populations there is a dearth of planets, and this area of the parameter space has been coined the hot-Neptune desert (e.g., Szabó & Kiss 2011; Beugé & Nesvorný 2013; Mazeh et al. 2016). The lack of planets found in this region cannot be explained by observational biases due to the large number of Neptunian-sized worlds found on longer orbits. Instead, the underpopulation of this regime has been hypothesized to be caused by photoevaporation whereby planets that spend significant time in these short orbits either have enough mass to remain a Jupiter-sized world or else have their primordial atmosphere completely eroded (e.g., Lundkvist et al. 2016; Lopez 2017).

LTT 9779 b (Jenkins et al. 2020) is an ultrahot Neptune discovered using data from TESS. With a period of less than a day and a radius of  $4.7 \pm 0.23 R_{\oplus}$ , LTT 9779 b lies within the hot-Neptune desert, as shown in Figure 1. Radial velocity

measurements have constrained the mass to  $29^{+0.78}_{-0.81} M_{\oplus}$ , yielding a density of  $1.536 \pm 0.123 \text{ g cm}^{-3}$ , which is suggestive of a gas-rich world. Given the rarity of worlds residing within the hot-Neptune desert, LTT 9779 b quickly became a target for atmospheric studies. Photometric eclipse observations of LTT 9779 b with Spitzer revealed a spectrum which is best fitted by a noninverted atmosphere and evidence was found for the presence of CO (Dragomir et al. 2020). Phase-curve observations with TESS and Spitzer have also revealed a large ( $\sim 1100 \text{ K}$ ) day–night temperature contrast and have suggested a supersolar atmospheric metallicity (Crossfield et al. 2020). However, the transit observations from these phase curves were not precise enough to constrain the molecular composition of the atmosphere in transmission. As part of a homogeneous population study of 70 gaseous exoplanets, Edwards et al. (2022) presented an HST WFC3 G141 transmission spectrum of LTT 9779 b. They found a spectrum with few obvious features except a slope of increasing transit depth with wavelength across the  $1.1\text{--}1.6 \mu\text{m}$  spectral range, which was best explained by a model with no molecular absorption, with the slope being instead best fit by collision-induced absorption (CIA) and Rayleigh scattering. Retrievals which included optical absorbers (TiO, VO, FeH, and H-) suggested the presence of TiO, but this was found to be strongly dependent upon the bluest spectral point and thus it was noted this could simply be noise.

In this paper, we present a new set of observations from HST WFC3 G102, reduced with the same methodology as in Edwards et al. (2022). The combined HST WFC3 G102 and G141 transmission spectrum of LTT 9779 b covers the wavelengths from  $0.8$  to  $1.6 \mu\text{m}$ . Analyzing these data, our free chemistry atmospheric retrievals prefer solutions with high abundances of  $\text{H}_2\text{O}$  and  $\text{CO}_2$ , with detection significances of  $3.11\sigma$  and  $2.35\sigma$ , respectively, as well as preferring the presence of FeH to  $2.12\sigma$ . The chemical equilibrium retrievals we conduct do not provide a preferable fit to the data than the free chemistry retrievals. Nevertheless, the best-fit solution suggests a carbon-to-oxygen ratio of  $\text{C/O} = 0.56^{+0.41}_{-0.34}$  and a very low atmospheric metallicity of  $\log(Z) = -2.74^{+0.69}_{-0.56}$ . Furthermore, we search for the  $1.083 \mu\text{m}$  helium line, but find no evidence for it within the HST data. Finally, we use the midtimes from the HST data, along with literature midtimes, to refine the period of LTT 9779 b and search for evidence of orbital decay or precession, finding no strong evidence that the orbital period is changing over the current observational baseline.

## 2. Methodology

HST WFC3 G102 and G141 observations of LTT 9779 b’s transit were taken as part of proposal GO-16457 (PI: Billy Edwards; Edwards et al. 2020a). These data were taken using the SPARS10 sequence and the GRISM256 aperture. The total exposure time was  $103.13 \text{ s}$ , with 16 up-the-ramp samples per exposure. Each visit consisted of four HST orbits, with the third occurring in transit. For wavelength calibration, a direct image with the F132N filter was taken at the start of the first orbit of each observation sequence. The spatial scanning technique (McCullough & MacKenty 2012) was utilized to increase the duty cycle and, thus, improve the S/N of the data. The scan ratio employed was  $0''.18 \text{ s}^{-1}$ , yielding a total scan length of  $19''.7$ , which equated to around 150 pixels.

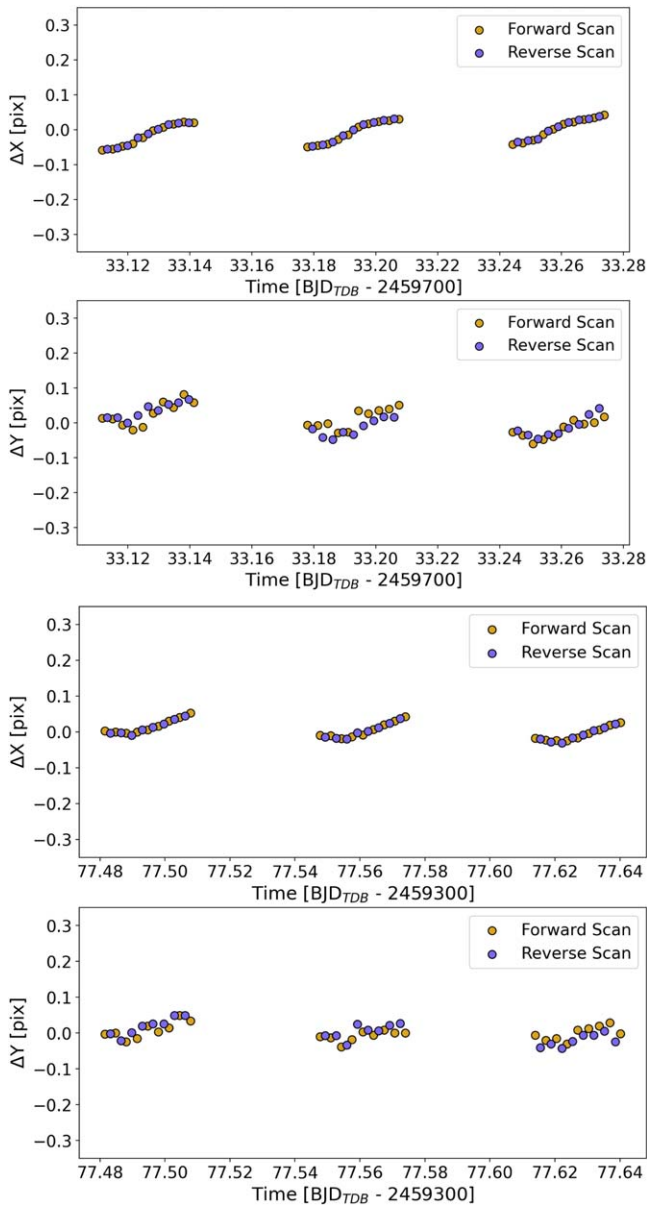


**Figure 2.** Shifts in the position of the spectrum on the detector in the spectral ( $x$ ) and spatial ( $y$ ) directions for the G102 (top) and G141 (bottom) visits. In both cases, the pointing across the visit was excellent.

### 2.1. Data Reduction and Light-curve Fitting

We carry out the analysis of the transit data using *Iraclis*, our highly specialized software for processing WFC3 spatially scanned spectroscopic images (Tsiaras et al. 2016a, 2016c, 2018), which has been used in a number of studies (e.g., Anisman et al. 2020; Changeat et al. 2020; Edwards et al. 2021; Libby-Roberts et al. 2022; Brande et al. 2022; Garcia et al. 2022). The reduction process includes the following steps: zero-read subtraction, reference-pixel correction, non-linearity correction, dark-current subtraction, gain conversion, sky-background subtraction, calibration, flat-field correction, and bad-pixel/cosmic-ray correction. Then we extract the white (1.088–1.680  $\mu\text{m}$ ) and the spectral light curves from the reduced images, taking into account the geometric distortions caused by the tilted detector of the WFC3 infrared channel. The pointing performance of HST was excellent across both visits

and Figure 2 shows the shift in the  $x$ - and  $y$ -position of the spectrum.

In the extraction of the flux from the calibrated images, *Iraclis* offers two techniques. The first extracts the flux from the image as it is at the end of the scan. The second splits the data into the up-the-ramp reads, subtracting each one sequentially from the next read and extracting the flux from each resulting image. The splitting extraction is useful for ensuring that there are no background stars with overlapping contributions to the target star’s spectrum. However, differences between the flux extracted with each method can also occur due to persistence. While the level of persistence is dependent upon the accumulated charge, it is also correlated with the time the charge has spent on the detector as well as the time since the last read (Anderson et al. 2014).

In the context of HST WFC3, this means the persistence is dependent upon the brightness of the host star, the scanning rate, and the readout scheme employed. We show this effect for the second forward scan of the second orbit (the first image used in the analysis) in Figure 3. The differences are clear when comparing the G102 data sets to those taken with the G141 grism: the persistence effect is greater in the latter case, likely due to the higher flux levels as the scan rate and readout schemes were identical. As the extracted flux using the full scan and splitting methods can be different, and to minimize the impact of persistence, we use the splitting extraction in this work.

We fit the light curves using our transit model package *PyLightcurve* (Tsiaras et al. 2016b) with the transit parameters from Table 2. The limb-darkening coefficients are calculated using *ExoTETHyS* (Morello et al. 2020) and based on the PHOENIX 2018 models from Allard et al. (2012). The stellar parameters used are also given in Table 2.

During our fitting of the white light curve, the planet-to-star radius ratio ( $R_p/R_s$ ) and the midtransit time ( $T_0$ ) were the only free parameters, along with the parameters used to model the systematics (Tsiaras et al. 2016c). It is common for WFC3 exoplanet observations to be affected by two kinds of time-dependent systematics: long-term and short-term “ramps.” The first affects each HST visit and is generally modeled as a linear behavior, while the second affects each HST orbit is modeled as having an exponential behavior (see, e.g., Kreidberg et al. 2014; Tsiaras et al. 2016c). The parametric model we use for the white light-curve systematics ( $R_w$ ) takes the form:

$$R_w(t) = n_w^{\text{scan}}(1 - r_a(t - T_0))(1 - r_{b1}e^{-r_{b2}(t-t_o)}), \quad (1)$$

where  $t$  is time,  $n_w^{\text{scan}}$  is a normalization factor,  $T_0$  is the midtransit time,  $t_o$  is the time when each HST orbit starts,  $r_a$  is the slope of a linear systematic trend along each HST visit, and ( $r_{b1}$ ,  $r_{b2}$ ) are the coefficients of an exponential systematic trend along each HST orbit. The normalization factor we use ( $n_w^{\text{scan}}$ ) is changed to  $n_w^{\text{for}}$  for upward-scanning directions (forward scanning) and to  $n_w^{\text{rev}}$  for downward-scanning directions (reverse scanning). The reason for using separate normalization factors is the slightly different effective exposure time due to the known upstream/downstream effect (McCullough & MacKenty 2012).

We fit the white light curves using the formulae above, considering the uncertainties per pixel as propagated through the data reduction process. However, it is common in HST/WFC3 data to have additional scatter that cannot be captured

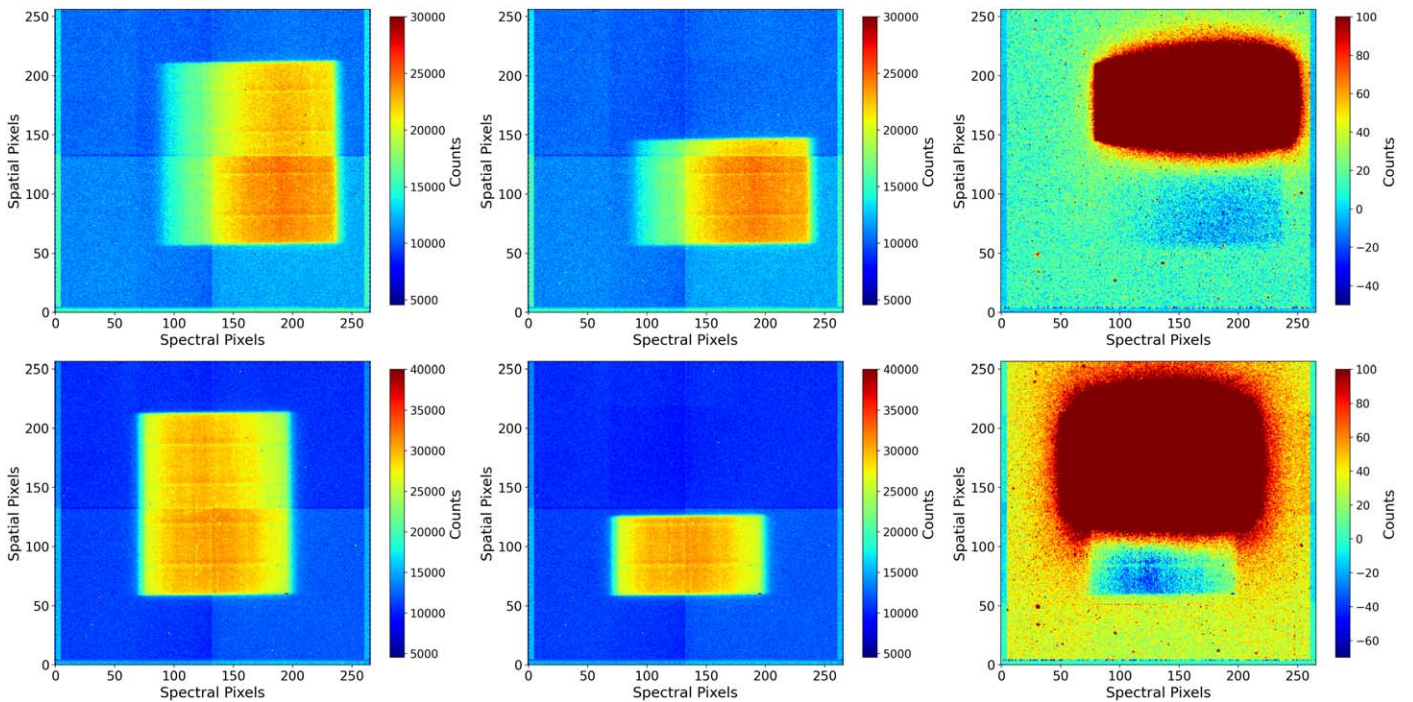


**Figure 3.** Raw images from the G102 (top) and G141 (bottom) observation sequences. In each case, the image illustrates the second forward scan of the second orbit, which is the first data set used in this analysis. For each panel, the left image shows the final read while the middle image displays a nondestructive read. The right image shows the flux levels once the nondestructive read is subtracted. The regions of negative flux highlight the persistence effect for these data sets. The color scale for the right images differ from the others in this figure to highlight this negative region.

by the ramp model. For this reason, we apply a scaling factor to each of the individual data point uncertainties to match their median to the standard deviation of the residuals and repeated the fitting (Tsiaras et al. 2018). The resulting fits for both the G102 and G141 observations are shown in Figure 4.

Next, we extract spectral light curves using the Iraclis “default\_high” binning for both grisms. We fit these spectral light curves with a transit model. In this case, the free parameters are the planet-to-star radius ratio and the parameters for the systematics model. The midtime was fixed to the best-fit value from the white light-curve fit while other orbital parameters were again fixed to those in Table 2. The systematics model,  $(R_\lambda)$ , includes the white light curve and a wavelength-dependent, visit-long slope (Tsiaras et al. 2016c), taking the form:

$$R_\lambda(t) = n_\lambda^{\text{scan}}(1 - \chi_\lambda(t - T_0)) \frac{\text{LC}_w}{M_w}, \quad (2)$$

where  $\chi_\lambda$  is the slope of a wavelength-dependent linear systematic trend along each HST visit,  $\text{LC}_w$  is the white light curve, and  $M_w$  is the best-fit model for the white light curve. Again, the normalization factor we use ( $n_\lambda^{\text{scan}}$ ) is changed to  $n_\lambda^{\text{for}}$  or  $n_\lambda^{\text{rev}}$  for the upward- or downward-scanning directions, respectively. Also, in the same way as for the white light curves, we perform an initial fit using the pipeline uncertainties and then refit while scaling up these uncertainties, such that their median matches the standard deviation of the residuals. The spectral light curves fits, for both visits, are given in Figure 5.

## 2.2. Atmospheric Retrievals

We explore the nature of LTT 9779 b’s lower atmosphere using Bayesian retrievals. These atmospheric retrievals are

performed on the extracted transmission spectrum using the publicly available retrieval suite `TauREx 3.1` (Al-Refaie et al. 2021, 2022).<sup>30</sup> In our retrievals, we assume that LTT 9779 b possesses a primary atmosphere with a solar ratio of helium to hydrogen ( $\text{He}/\text{H}_2 = 0.17$ ). The atmosphere of LTT 9779 b is simulated to range from  $10^{-4}$  to  $10^6$  Pa ( $10^{-9}$  to 10 bar) and sampled uniformly in log-space by 100 atmospheric layers. The retrieved radius is, therefore, the 10 bar radius. We include CIA from  $\text{H}_2$ – $\text{H}_2$  (Abel et al. 2011; Fletcher et al. 2018) and  $\text{H}_2$ – $\text{He}$  (Abel et al. 2012) as well as Rayleigh scattering for all molecules. We model clouds as a uniform opaque deck, fitting only the cloud-top pressure (i.e., gray clouds). We then perform two main types of retrievals, those which fit each molecular species independently (i.e., free chemistry) and those which assume the molecules to be in chemical equilibrium.

For the free chemistry retrievals, we include the molecular opacities from the ExoMol (Tennyson et al. 2016), HITRAN (Gordon et al. 2016), and HITEMP (Rothman & Gordon 2014) databases. Based on the expected chemical species of such a hot planet, we include the opacities of  $\text{H}_2\text{O}$  (Polyansky et al. 2018),  $\text{CO}$  (Li et al. 2015),  $\text{CO}_2$  (Rothman et al. 2010),  $\text{HCN}$  (Barber et al. 2013),  $\text{TiO}$  (McKemmish et al. 2019),  $\text{VO}$  (McKemmish et al. 2016),  $\text{FeH}$  (Wende et al. 2010), and  $\text{H}^-$  (John 1988). To implement the last of these, we use the methodology described in Edwards et al. (2020b), fixing the neutral hydrogen volume mixing ratio and thus only fitting for the  $e^-$  volume mixing ratio. We note that Himes & Harrington (2022) showed that Equation (3) from John (1988) does not replicate the table of coefficients in that same paper. Himes & Harrington (2022) recommend using Table 1 from John (1988), which is what is implemented here.

<sup>30</sup> [https://github.com/ucl-exoplanets/TauREx3\\_public](https://github.com/ucl-exoplanets/TauREx3_public)

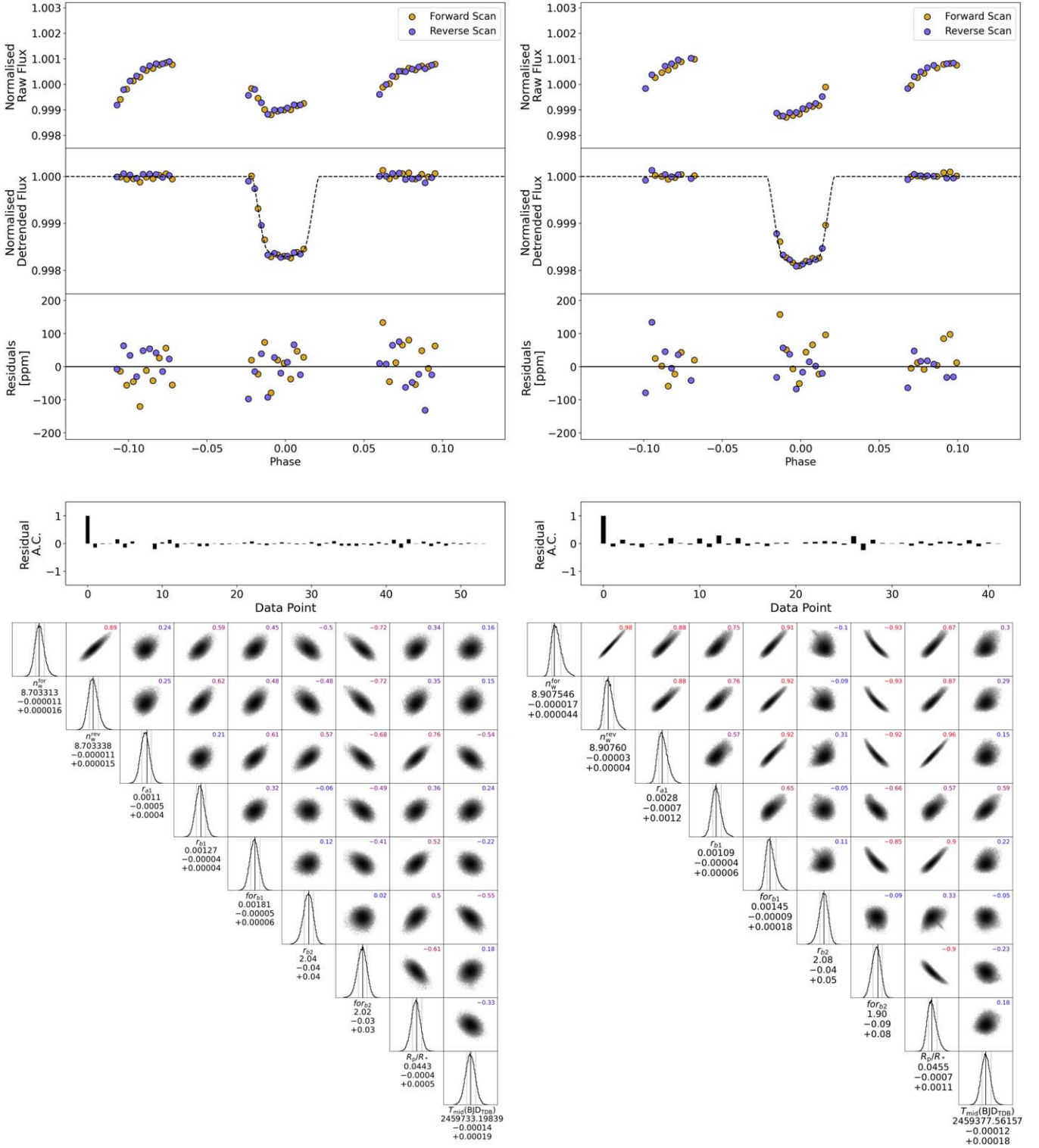


**Figure 4.** White light-curve fits for the HST WFC3 G102 (left) and G141 (right) data of LTT 9779 b. In each case, the top plot shows the raw light curve (top panel), corrected light curve and best-fit model (second panel), the residuals having removed the best-fit model (third panel), and the AC function (bottom panel). The lower graphic is a corner plot for the fit. As with the majority of HST data sets, there is a correlation between the white light-curve depth and the parameters for the systematics (Equation (1)), thereby indicating that achieving absolute transit depths is difficult with these data. For the data studied here, the G141 data show the highest correlation. Nevertheless, no major offset in the transit depth was found between the two visits.

In each free chemistry case, all molecular abundances are allowed to vary from  $\log(\text{VMR}) = -1$  to  $\log(\text{VMR}) = -15$ . Higher mixing is not expected in the hydrogen-dominated atmosphere of LTT 9779 b and, in any case, these would also necessitate accounting for self-broadening of the molecular lines

(Anisman et al. 2022a, 2022b). We explore using both an isothermal temperature profile and an NPoint profile. For the former, we fit only the temperature. For the later, we fit the temperature at the “surface” (10 bar) and the temperature at the “top” of the atmosphere ( $10^{-9}$  bar) as well as two intermediary

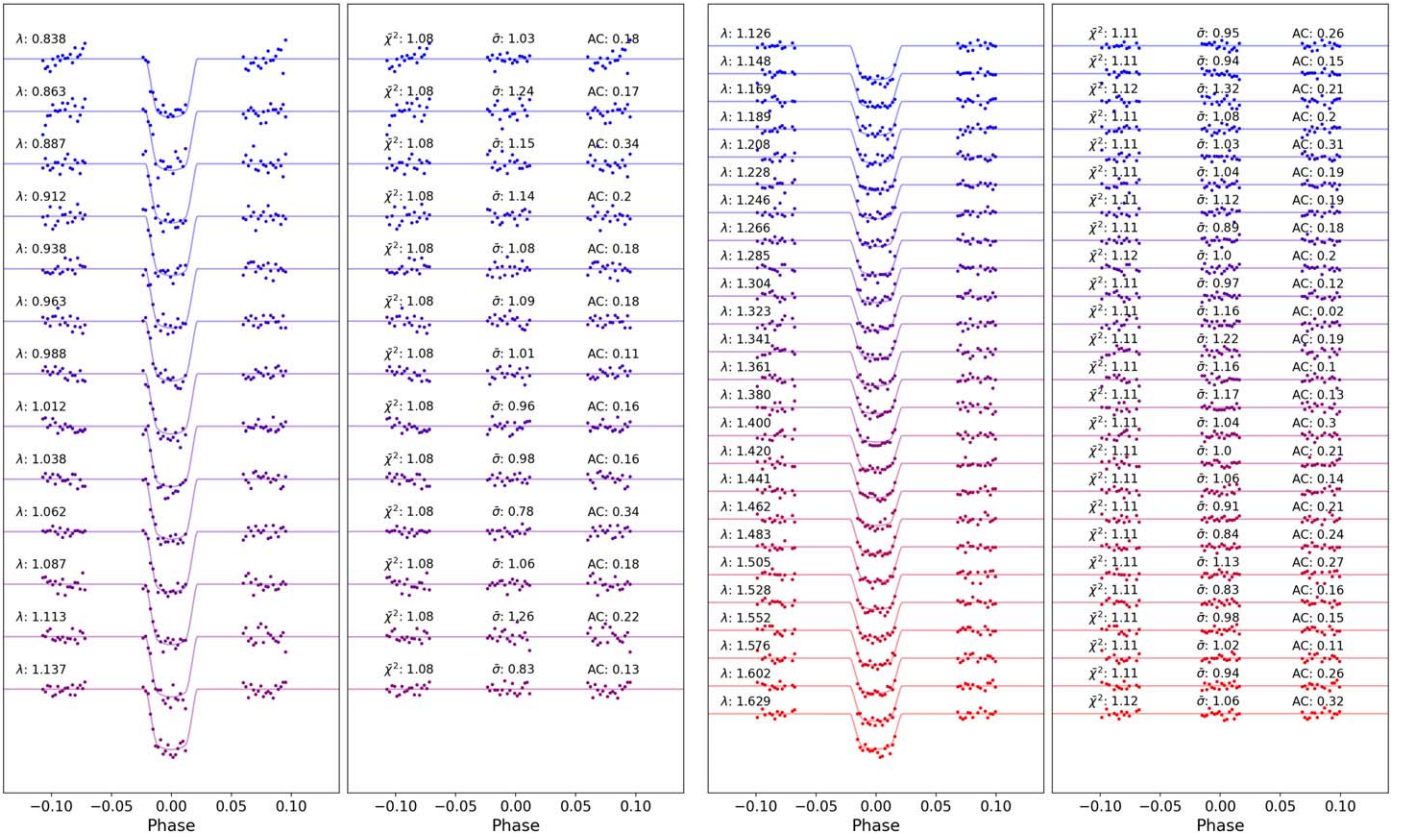


**Figure 5.** Spectral light curves fitted with *Traculis* for the G102 (left) and G141 (right) observations of LTT 9779 b where, for clarity, an offset has been applied. Each plot shows the detrended spectral light curves with the best-fit model plotted (left) as well as the residuals from the fitting (right). The values for the reduced chi-squared ( $\chi^2$ ), the standard deviation of the residuals with respect to the photon noise ( $\sigma$ ), and the autocorrelation (AC) function are also shown.

points. For these intermediary points, we also fit the pressure at which these points occur. Therefore, the isothermal profile adds only a single free parameter to the retrieval while the NPoint adds six. For the free chemistry retrievals, we explore both chemical profiles which were constant with altitude and more complex, varying with altitude, two-layer profiles (Changeat et al. 2019).

Additionally, we conduct equilibrium chemistry retrievals using the code *GGchem* (Woitke et al. 2018) via the *TauREx* plug-in system (Al-Refaie et al. 2022). As with the free chemistry retrievals, we include Rayleigh scattering and CIA as well as simple gray clouds. For these retrievals, the free chemical parameters are the atmospheric metallicity and C/O ratio. For the equilibrium chemistry retrievals, the metallicity is allowed to vary from  $10^{-4}$  to  $10^4$  and the C/O ratio has bounds of  $10^{-3}$  and 2.

Recovering absolute transit depths is difficult, particularly given the strong systematics present within HST observations (e.g., Changeat et al. 2020; Guo et al. 2020). Therefore, one can induce offsets in the transit depth between data sets from different instruments<sup>31</sup> which, if left uncorrected, could bias the retrieved atmospheric composition. Hence, we also conduct retrievals where we allow the G141 data set to be shifted relative to the G102 data, with this offset being a free parameter in the retrieval (e.g., Luque et al. 2020; Yip et al. 2021). We allow the G141 data to be shifted due to the strong correlations between the transit depth and systematics model (see Figure 4). To allow for this possibility to be fully explored, the bounds for this offset are set to be extremely broad:  $\pm 10^{-2}$  (10,000 ppm).

<sup>31</sup> Offsets are also found between different observations with the same instrument, see, e.g., Edwards et al. (2022).

Stellar activity, in the form of photospheric heterogeneities (i.e., spots and faculae), can contaminate the transmission spectrum of an exoplanet (e.g., Ballerini et al. 2012; McCullough et al. 2014; Rackham et al. 2018; Barclay et al. 2021). The contamination introduced is strongly chromatic with the strongest effects seen at shorter, optical wavelengths. As such, the possibility of stellar contamination is particularly important to consider for the G102 observations. Hence, we conduct retrievals using the Active Stellar Retrieval Algorithm (*ASteRA*) plug-in for *TauREx*, outlined in Thompson et al. (2023), to explore potential contamination in the case of LTT 9779 b. In our setup, we allow for possible contamination effects due to both unocculted spots and unocculted faculae. *ASteRA* requires four additional fitting parameters, which are the spot and faculae temperatures,  $T_{\text{Spot}}$  and  $T_{\text{Fac}}$ , respectively, and their respective filling factors,  $F_{\text{Spot}}$  and  $F_{\text{Fac}}$ . We again use intentionally unrestrictive priors, with  $F_{\text{Spot}}$  and  $F_{\text{Fac}}$  bounds of 0 and 0.99,  $T_{\text{Spot}}$  bounds of 4000 and 5440 K and  $T_{\text{Fac}}$  bounds of 5450–6000 K.

Finally, we explore the parameter space using the nested sampling algorithm *Multinest* (Feroz et al. 2009; Buchner et al. 2014) with 1000 live points and an evidence tolerance of 0.5. We then utilize the Bayesian evidence derived by *Multinest* as a means of selecting the preferred atmospheric model and for judging the significance of molecular detections.

### 2.3. Probing Atmospheric Mass Loss via the Helium Line at $1.083 \mu\text{m}$

Close-in gaseous planets are expected to be undergoing atmospheric escape due to the high levels of stellar irradiation.

Indeed, hydrodynamic escape has been proposed as the cause of the dearth of hot Neptunes, with planets either being completely stripped or having a high-enough starting mass to retain the majority of their primordial envelope (e.g., Lundkvist et al. 2016; Mazeh et al. 2016).

Observational studies have been undertaken in an attempt to detect atmospheric escape and constrain the rate of mass loss. Many of these have focused on using the Ly $\alpha$  line, but despite these successes, attenuation by neutral hydrogen in the interstellar medium removes the majority of the Ly $\alpha$  line profile and so other tracers of mass loss have also been proposed. One such alternative line is that of metastable helium which occurs at 1.083  $\mu\text{m}$  (Oklopčić & Hirata 2018). Ground-based observations have had notable success in detecting escape via this observable (e.g., Allart et al. 2018; Nortmann et al. 2018; Zhang et al. 2023), but the first detection of helium came via observations with HST. The G102 grism of WFC3 was used to observe WASP-107 b (Anderson et al. 2017), with an excess absorption being detected around 1.083  $\mu\text{m}$  (Spake et al. 2018). These data suggested a mass-loss rate of  $10^{10}$ – $3 \times 10^{11}$   $\text{g s}^{-1}$ . Similarly, HST WFC3 G102 data of HAT-P-11 b found evidence for a mass-loss rate of  $10^9$ – $10^{11}$   $\text{g s}^{-1}$  (Mansfield et al. 2018) although high-resolution ground-based observations suggested a lower mass-loss rate (Allart et al. 2018). Observations of the helium triplet have also been undertaken for planets on the edge of the hot-Neptune desert, with the resulting mass-loss rates suggesting that the upper edge (i.e., higher-mass planets) of the desert is impervious to atmospheric escape (Vissapragada et al. 2022).

As LTT 9779 b lies within the rarely populated hot-Neptune desert it is expected that atmospheric loss should be ongoing, despite the old age of the system. Therefore, as well as using the HST WFC3 G102 data to constrain the atmospheric composition via a low-resolution spectrum, we also extract a higher-resolution spectrum to search for evidence of mass loss via the helium line. Using the excellent wavelength calibration offered by *Iraclis*, we extract overlapping bins with a bandwidth of 3 nm (30  $\text{\AA}$ ) and a separation of 0.1  $\text{\AA}$  across the entire G102 range and perform fits to each of these light curves in the same way as discussed in Section 2.1. We then use the transit depths recovered in these overlapping bins to search for excess absorption around 1.083  $\mu\text{m}$ .

Separately, we estimate the expected atmospheric escape rate using a photoevaporation model (A. Allan et al. 2023, submitted). In our model, the high-energy stellar radiation ionizes hydrogen and helium atoms, and the excess energy released after the ionization heats the planet’s upper atmosphere, which more easily evaporates. We construct the incoming high-energy stellar spectrum of LTT 9779 using HST Space Telescope Imaging Spectrograph (STIS) near-ultraviolet (NUV)/optical observations (G230L and G430L) that were taken as part of the MUSCLES Extension for Atmospheric Transmission Spectroscopy program (GO-16166; PI: Kevin France; France et al. 2020). As LTT 9779 is a Sun-like star (Jenkins et al. 2020), the far-ultraviolet (FUV) portion of the spectrum (1170–2200  $\text{\AA}$ ) is assumed to be the spectrum of the quiet Sun (Woods et al. 2009), scaled to the HST STIS G230L spectrum of LTT 9779; the adopted scaling factor was  $9.0519 \times 10^{-16}$ . Meanwhile, the HST STIS G140M data are utilized to reconstruct Ly $\alpha$  using the methodology described in Youngblood et al. (2022). The Ly $\alpha$  flux is then used to compute the extreme-ultraviolet (EUV; 100–1170  $\text{\AA}$ ) flux of

LTT 9779 using the scaling relations from Linsky et al. (2014). Finally, as X-ray observations with Chandra led to a nondetection, we also use a scaled solar X-ray spectrum (5–100  $\text{\AA}$ ).

Our atmospheric escape model requires as input the incident flux in four energy bins, X-ray (0.517–1.24 nm), hard EUV (10–36 nm), soft EUV (36–92 nm) and FUV+NUV (91.2–320 nm). By integrating the spectrum above, the luminosities of each of these bins are  $3.35 \times 10^{26}$ ,  $3.02 \times 10^{27}$ ,  $2.30 \times 10^{27}$ , and  $2.22 \times 10^{31}$   $\text{erg s}^{-1}$ , respectively. Our model then solves for the hydrodynamics equations (conservation of mass, momentum, and energy) and ionization balance of hydrogen (Allan & Vidotto 2019). In our most recent model version (A. Allan et al. 2023, submitted), we also self-consistently compute the helium population (neutral helium in the singlet and triplet states, as well as ionized helium), and their corresponding energetics. The helium abundance is an input parameter of our model and we run two models, the first assuming an abundance by number of 2% and a second at 10%.

#### 2.4. Updated Ephemeris and Search for Orbital Decay or Precession

Maintaining exoplanet ephemerides is crucial for ensuring that atmospheric studies of exoplanets can be undertaken. Therefore, we utilize the midtimes from our HST light-curve fits, as well as literature observations, to refine the period of LTT 9779 b. Data from TESS Sector 2 led to the discovery of LTT 9779 b and it has since reobserved the host star in Sector 29.<sup>32</sup> These TESS data were analyzed by Kokori et al. (2023) as part of the ExoClock project (Kokori et al. 2021, 2022), which aims to refine the ephemerides of planets which will be studied by the Ariel mission (Tinetti et al. 2018, 2021; Edwards et al. 2019). In our work, we took the TESS midtimes from this previous study and incorporated new unpublished TESS eclipses. As with Kokori et al. (2023), we utilize the 2 minute cadence Presearch Data Conditioning (PDC) light curves (Smith et al. 2012; Stumpe et al. 2012, 2014). Due to the poor S/Ns of the TESS eclipses, we fit them in groups of four eclipses to achieve eclipse midtime uncertainties that were of a similar precision to the transit measurements. Furthermore, before the end of operations, Spitzer observed eclipses and phase curves of LTT 9779 b (Crossfield et al. 2020; Dragomir et al. 2020). We combine the midtimes from these studies with our data to extend the number of epochs during which LTT 9779 b has been observed. A full list of the midtimes utilized here are given in the Appendix in Tables 4 and 5.

To constrain the orbital period further, we utilize the radial velocity data taken of LTT 9779 by CORALIE and HARPS, which were presented in the detection paper of the planet (Jenkins et al. 2020). To model the radial velocity profile, we use *RadVel* (Fulton et al. 2018). The radial velocity data and the transit midtimes are fitted under one likelihood using *MultiNest* (Feroz et al. 2009; Buchner et al. 2014) to explore the parameter space. For the linear ephemeris model, we assume a circular orbit ( $e = 0$ ) following the conclusions of Jenkins et al. (2020).

Given the short period of LTT 9779 b, one might expect that the planet’s orbit should be shrinking gradually over time due to the transfer of angular momentum from the planet to the host

<sup>32</sup> We note that LTT 9779 will also be studied in TESS Sector 69 (2023 August–September).

star, eventually leading to planetary engulfment. This may occur when the orbital period of a planet is shorter than the rotational period of its host star, as is the case for LTT 9779 b (Jenkins et al. 2020). In this scenario the star’s tidal bulge lags behind the tidal bulge of the planet, generating a net torque that spins up the star and causes the planet to spiral inwards (Levrard et al. 2009; Matsumura et al. 2010). For a given arrangement, the rate of the decay of the orbital period is dependent on the efficiency of tidal energy dissipation within the star, parameterized by the modified stellar tidal quality factor  $Q'_*$  (Penev et al. 2018). Directly measuring the orbital decay rate via long-term transit timing measurements provides an estimate of  $Q'_*$ , with a larger value being associated with less efficient dissipation and therefore a slower decay rate. While many studies have searched for evidence of orbital decay (e.g., Patra et al. 2020; Hagey et al. 2022), the only highly convincing detection so far has been for WASP-12 b (e.g., Maciejewski et al. 2016; Patra et al. 2017; Yee et al. 2019; Turner et al. 2020; Wong et al. 2022).

Therefore, in addition to fitting the timing data with a constant-period model, we fit an orbital decay model to the midtimes and radial velocity data of LTT 9779 b. For a planet on a Keplerian circular orbit with a constant orbital period  $P$ , we expect the central time of the transits  $t_{\text{tra}}$  and the occultations  $t_{\text{occ}}$  to increase linearly. Therefore, these can be described by:

$$t_{\text{tra}} = t_0 + PE \text{ and} \quad (3)$$

$$t_{\text{occ}} = t_0 + \frac{P}{2} + PE, \quad (4)$$

where  $t_0$  is the midtransit time of the reference epoch and  $E$  is the orbit number. In the case of orbital decay, the gradual shrinking of the orbital period gives rise to nonlinear drift in the observable transit and eclipse midtimes. The simplest way to represent this behavior is to include a quadratic term in the expected transit and eclipse center times. The model is given by:

$$t_{\text{tra}} = t_0 + PE + \frac{1}{2} \frac{dP}{dE} E^2 \text{ and} \quad (5)$$

$$t_{\text{occ}} = t_0 + \frac{P}{2} + PE + \frac{1}{2} \frac{dP}{dE} E^2, \quad (6)$$

where  $\frac{dP}{dE}$  is the period derivative, which we assume to be constant. If negative, it signifies that the orbit of the planet is decaying. We again sample the parameter space using `Multinest` and compare the Bayesian evidence between each fit to determine the preferred model. The constant-period model has two free parameters: the reference epoch  $t_0$  and the period  $P$ . The decay model has three parameters, adding the  $dP/dE$  term. As we fit the midtimes and radial velocity data simultaneously, each model has the additional radial velocity model parameters of the velocity semiamplitude ( $K$ ) and systemic velocities of HARPS ( $V_{\text{H}}$ ) and Coralie ( $V_{\text{C}}$ ).

On the other hand, if the orbit of LTT 9779 b is slightly eccentric, one may expect the argument of periape to precess over time due to a number of effects (see Section 4.2) which would induce sinusoidal variations in the transit and eclipse timing. Hence, we also attempt to fit an apsidal precession model to the timing data. In this case, the transit and eclipse

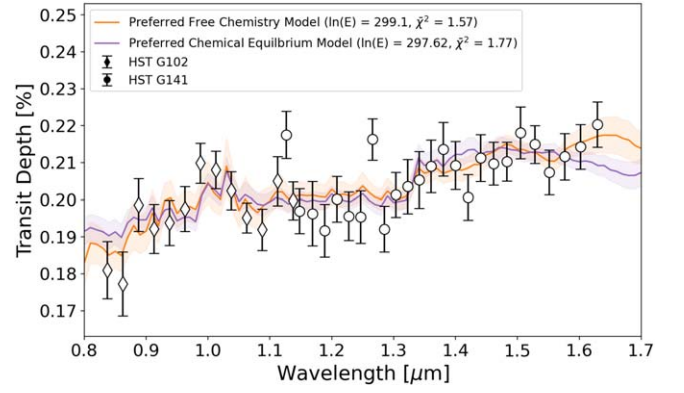


**Figure 6.** The obtained spectrum from HST WFC3 G102 and G141. Overplotted are the preferred free chemistry (orange) and chemical equilibrium (purple) models. Based on the Bayesian evidence, the free chemistry model is preferred by  $2.4\sigma$ .

times can be expressed as:

$$t_{\text{tra}} = t_0 + P_s E - \frac{e P_a}{\pi} \cos \omega, \quad (7)$$

$$t_{\text{occ}} = t_0 + \frac{P_a}{2} + P_s E + \frac{e P_a}{\pi} \cos \omega, \quad (8)$$

$$\omega(E) = \omega_0 + \frac{d\omega}{dE} E, \text{ and} \quad (9)$$

$$P_s = P_a \left( 1 - \frac{d\omega/dE}{2\pi} \right), \quad (10)$$

for argument of pericenter  $\omega$ , phase  $\omega_0$ , and precession rate  $d\omega/dE$ . In these equations,  $P_s$  represents the planet’s sidereal period, which is assumed to be fixed, while  $P_a$  is the “anomalous” period. This latter period is also fixed, but accounts for the additional period signal due to precession. We note that this approach is an approximation and is only valid for  $e \ll 0.1$  (Ragozzine & Wolf 2009), but, given the very short period of LTT 9779 b and an upper limit of  $e < 0.058$  at 95% confidence from Jenkins et al. (2020), this assumption is valid in this scenario. For the precession model there are a total of eight free parameters ( $t_0$ ,  $P$ ,  $\omega_0$ ,  $d\omega/dE$ ,  $e$ ,  $K$ ,  $V_{\text{H}}$ , and  $V_{\text{C}}$ ).

### 3. Results

#### 3.1. Atmospheric Composition

We conduct a number of atmospheric retrievals using `TauREx 3.1` using both free chemistry and chemical equilibrium models. Based on the Bayesian evidence, the preferred model is a free chemistry retrieval which assumed an isothermal atmosphere and for abundances of  $\text{H}_2\text{O}$  and  $\text{CO}_2$  that changed with altitude. The model is preferred to that with constant chemical abundances by  $2.41\sigma$ . The preference between this free model and the chemical equilibrium retrieval with a nonisothermal temperature profile is  $2.40\sigma$ . The nonisothermal chemical equilibrium retrieval is preferred to its isothermal counterpart by  $2.48\sigma$ . We show the best-fit spectra for the preferred free and chemical equilibrium models in Figure 6.

Our preferred free chemistry retrieval favors the presence of  $\text{H}_2\text{O}$ ,  $\text{CO}_2$ , and  $\text{FeH}$  while also placing upper limits on the presence of  $\text{TiO}$  and  $\text{VO}$ . The retrieved abundances for our preferred free and chemical equilibrium retrievals are compared

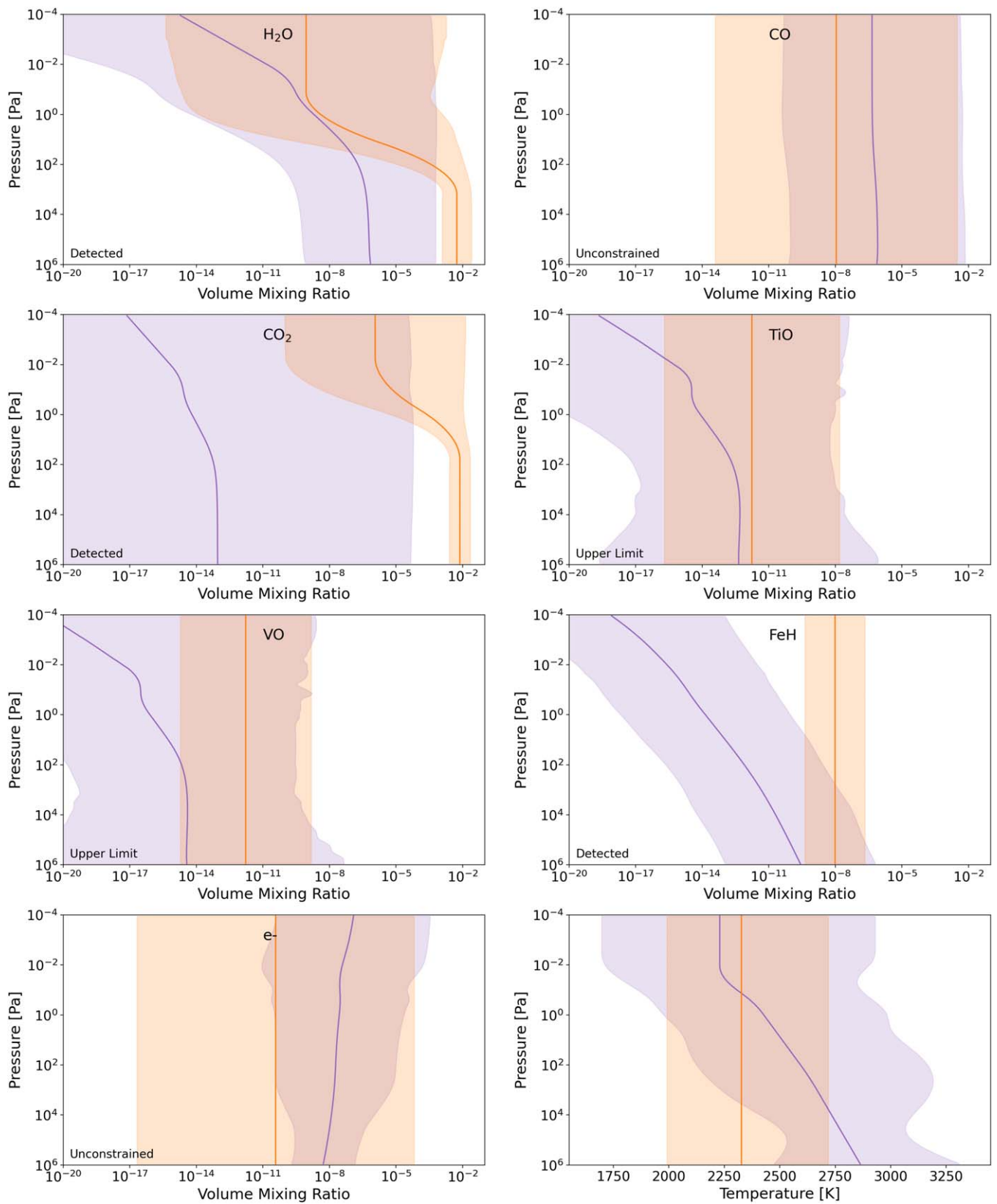


**Figure 7.** Retrieved molecular abundances from free chemistry (orange) and chemical equilibrium (purple) retrievals. Our free chemistry retrievals suggest the presence of H<sub>2</sub>O, CO<sub>2</sub>, and FeH. They also place upper limits on the abundances of TiO and VO but could not constrain CO or e<sup>-</sup>. The preferred abundance of CO<sub>2</sub> is very different between the models, as is the H<sub>2</sub>O abundance in the lower atmosphere. The retrieved temperature profiles also slightly differ, but are generally within 1 $\sigma$ .

**Table 1**  
Summary of the Atmospheric Retrievals Conducted in This Work

Chemistry	TP Profile	Molecules Removed <sup>a</sup>	Two-layer Molecules	Offset	Spots/Fac	$\ln(E)$	$\bar{\chi}^2$
Free	Isothermal	None	H <sub>2</sub> O and CO <sub>2</sub>	False	False	299.10	1.57
Free	Isothermal	H <sub>2</sub> O	CO <sub>2</sub>	False	False	295.64	1.74
Free	Isothermal	CO <sub>2</sub>	H <sub>2</sub> O	False	False	297.51	1.62
Free	Isothermal	FeH	H <sub>2</sub> O and CO <sub>2</sub>	False	False	297.93	1.73
Free	Isothermal	None	None	False	False	297.77	1.46
Free	Isothermal	None	H <sub>2</sub> O and CO <sub>2</sub>	False	True	299.31	2.43
Free	Isothermal	None	H <sub>2</sub> O and CO <sub>2</sub>	True	False	293.76	1.68
Free	NPoint	None	H <sub>2</sub> O and CO <sub>2</sub>	False	False	298.32	2.15
Free	NPoint	None	H <sub>2</sub> O and CO <sub>2</sub>	True	False	294.98	2.27
Free	NPoint	None	None	False	False	297.61	1.87
Chem Eq	Isothermal	N/A	N/A	False	False	295.74	1.57
Chem Eq	NPoint	N/A	N/A	False	False	297.62	1.77
Chem Eq	NPoint	N/A	N/A	True	False	293.30	1.90

**Note.**

<sup>a</sup> Compared to the standard setup of H<sub>2</sub>O, CO<sub>2</sub>, CO, HCN, TiO, VO, FeH, and H<sup>+</sup>.

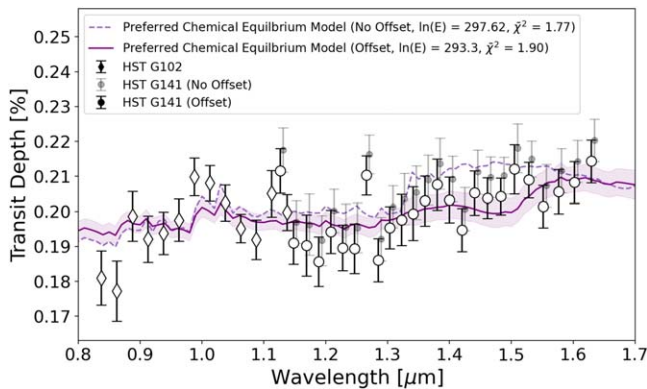


**Figure 8.** Spectrum from the chemical equilibrium retrieval which included an offset for the HST WFC3 G141 data. The retrieval preferred to reduce the depth of the G141 data by 60 ppm but the solution is not preferred over a retrieval without an offset.

in Figure 7. While many of the abundances agree across these two models, the CO<sub>2</sub> abundance is far higher in the free chemistry case, with the H<sub>2</sub>O abundance in the lower half of the atmosphere also being noticeably higher. While our models preferred the presence of CO<sub>2</sub>, WFC3 data only have limited sensitivity to carbon-bearing species and this can mean that the molecules retrieved are very dependent upon how the retrieval is set up (e.g., Changeat et al. 2020).

Our preferred chemical equilibrium retrieval is that which uses a nonisothermal profile. It is likely that this allows for the model to have more flexibility in the dissociation of molecules with altitude compared to when an isothermal profile is used. However, when comparing the retrieved metallicity and C/O ratio we find that the temperature profile did not overly impact the results (see Figure 9). We note again that the HST WFC3 range does not give a strong sensitivity to carbon-bearing species and so the C/O ratio is not only poorly constrained but also not likely to be trustworthy (Rocchetto et al. 2016).

Spectral data from different instruments and epochs cannot be automatically assumed to be compatible. Recovering absolute transit depths is extremely difficult and the corner plots of the white light-curve fit for the HST WFC3 G141 observations (Figure 4) show a clear correlation between the

transit depth and the systematics model. Therefore, despite the data sets seemingly being compatible when plotted together, we also perform retrievals which allow a global offset to be applied to the G141 data. For these, we utilize the setups from our preferred free chemistry and chemical equilibrium retrievals, with the only change being the addition of this offset parameter.

We find that, in the free chemistry case, the retrieval converges to a solution with a slight offset. However, given the  $1\sigma$  uncertainties on this parameter, it is also consistent with there being no offset ( $-10^{+33}_{-38}$  ppm). Meanwhile, the chemical equilibrium retrieval prefers a more significant offset ( $-60 \pm 26$  ppm) and we show the preferred solution, including the offset to the HST WFC3 G141 data, in Figure 8. However, in both cases, the Bayesian evidence shows that the models without offsets were preferred by  $3.96\sigma$  and  $3.4\sigma$  for the free and chemical equilibrium cases, respectively.

Due to the slope of the spectrum, we investigate the possibility that unocculted spots and faculae are the cause of the modulation seen. Unocculted faculae in particular are capable of reproducing the observed negative blueward slope. Our free chemistry retrievals in which this effect was accounted for lead to a fit which has a highly similar Bayesian evidence to that of the free chemistry model alone but requires four additional fitting parameters. The inclusion of the modeling of stellar heterogeneities removes any strong constraints on the atmosphere, with no molecules being conclusively detected. However, the retrieval converges to an extremely high faculae filling factor ( $65\% \pm 12\%$  of the unocculted stellar surface). Given that the star is known to be slowly rotating and therefore inactive (Jenkins et al. 2020), and that there have been no indications of occulted faculae in any transit observations taken of the LTT 9779 b, this value is likely unrealistic.

We provide an overview of our retrieval setups, as well as the associated evidence and reduced chi-square values, in Table 1.

### 3.2. Search for the 1.083 $\mu\text{m}$ Helium Line

As well as the low-resolution spectrum used for our atmospheric retrievals, we also extract a higher-resolution spectrum using the G102 data with the aim of searching for the helium line at 1.083  $\mu\text{m}$  that would be indicative of ongoing

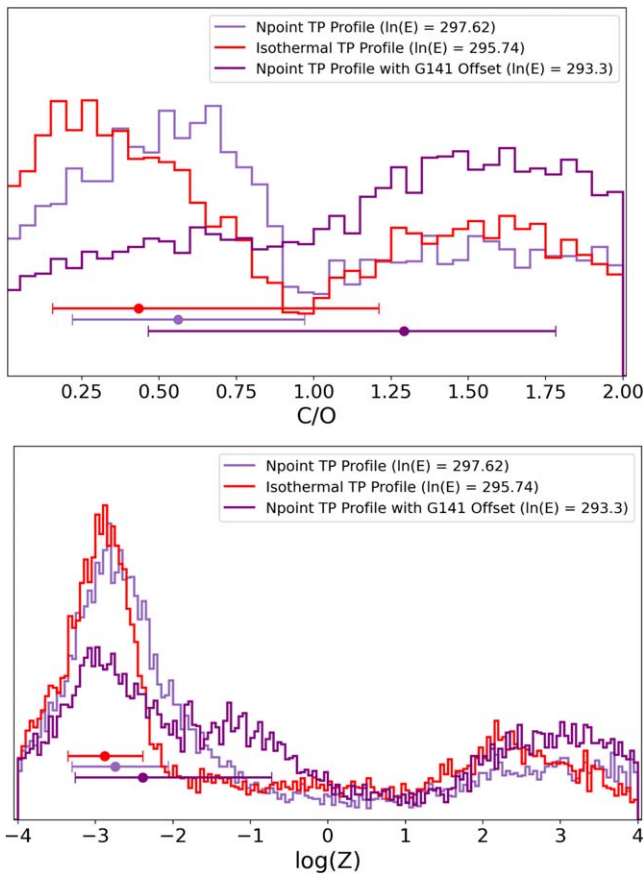


**Figure 9.** Probability distributions for the C/O (top) and atmospheric metallicity ( $\log_{10}(Z)$ , bottom) from the different chemical equilibrium retrievals conducted here. The constraints placed on these properties are poor in each case, but all three prefer solutions with very low atmospheric metallicities.

mass loss. However, despite sampling this spectral range with overlapping spectral bins which had a spacing of only  $0.1 \text{ \AA}$  and a bandwidth of  $3 \text{ nm}$  ( $30 \text{ \AA}$ ), we find no obvious evidence of excess absorption at, or around, this wavelength (see the top panel of Figure 10). The variations that are seen in this spectrum are likely due to correlated noise.

We also model the predicted atmospheric evaporation using the methods of Allan & Vidotto (2019) and the reconstructed high-energy spectrum of LTT 9779 presented in Section 2.3. We find that assuming either a 2/98 or 10/90 helium to hydrogen number abundance, the evaporation rate is expected to be  $\sim 10^{11} \text{ g s}^{-1}$ , reaching velocities of up to  $\sim 50 \text{ km s}^{-1}$ . However, even though the planet is anticipated to have a substantial evaporation rate driven by photoionization, the expected signature of the evaporation in the triplet lines is very small, particularly in the 2/98 case. The middle panels of Figure 10 show the anticipated transmission spectrum in the helium triplet, where we derive a peak transit depth of 0.29%. Due to the width of the spectral bins ( $3 \text{ nm}/30 \text{ \AA}$ ), the helium triplet would not appear as a sharp peak but as a plateau in the data: multiple bins would completely contain the excess absorption. In the bottom panel of Figure 10 we show the magnitude of this plateau when our 10/90 He/H model is convolved with these spectral bins. Even in the 10/90 case, the expected signature strength is far smaller than the uncertainties on the G102 spectral data ( $\sim 20 \text{ ppm}$  versus  $\sim 135 \text{ ppm}$ ). Therefore, we conclude the data are not sufficient to detect this tracer as even though we expect LTT 9779 b has a significant

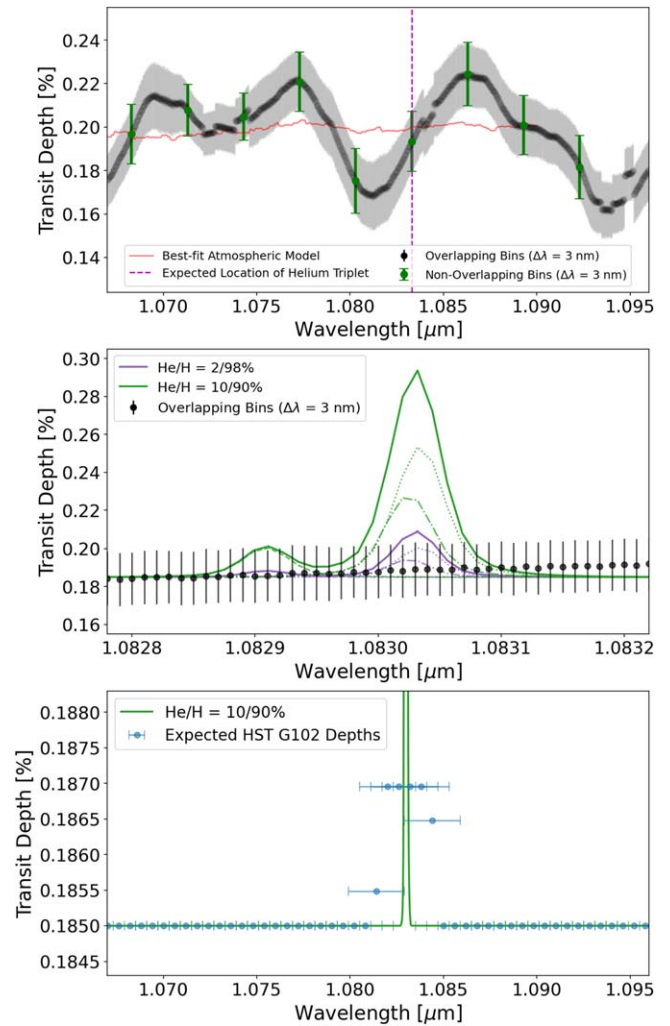


**Figure 10.** Search for the  $1.083 \mu\text{m}$  helium triplet. While it is expected that the planet is undergoing mass loss, little evidence could be found via this tracer with the data collected with HST WFC3 G102. Top: the higher-resolution HST WFC3 G102 spectrum extracted in this work. The bins are spaced by  $0.1 \text{ \AA}$  but have a bandwidth of  $3 \text{ nm}$  and, therefore, are overlapping. The location of the peak of the helium triplet signature is indicated by the purple dashed line. The best-fit atmospheric model from Section 3.1 is also shown (red) for context, as are a set of bins which are not overlapping (green). Middle: expected signal of the helium triplet derived from simulations of atmospheric escape driven by photoevaporation (A. Allan et al. 2023, submitted). The line is formed of three segments (dotted, dashed, and dotted-dashed) which together produce the final signal (solid). The expected triplet signature is shown for two He/H ratios. The HST WFC3 G102 data are also shown, with no excess absorption seen in these bins. Bottom: our simulated helium signature when convolved with the bins extracted. As the spectral bins are overlapping, the expected signal in these bins from the triplet appears as a plateau. The size of the signal ( $\sim 20 \text{ ppm}$ ) is much smaller than the uncertainties on each data point ( $\sim 135 \text{ ppm}$ ), even in the 10/90 He/H case. Thus we conclude that the data are not sensitive enough to detect the expected triplet signature.

evaporation rate, its evaporation is barely seen in the helium triplet.

### 3.3. Updated Ephemeris and Search for Long-term Timing Variations

We fit the transit and eclipse midtimes with three models: linear ephemeris, orbital decay, and apsidal precession. We find no statistical evidence to prefer orbital decay over a linear ephemeris: the linear model has a Bayesian log evidence of  $\ln(E) = -225.1$  while the decay yielded  $\ln(E) = -224.9$ . The

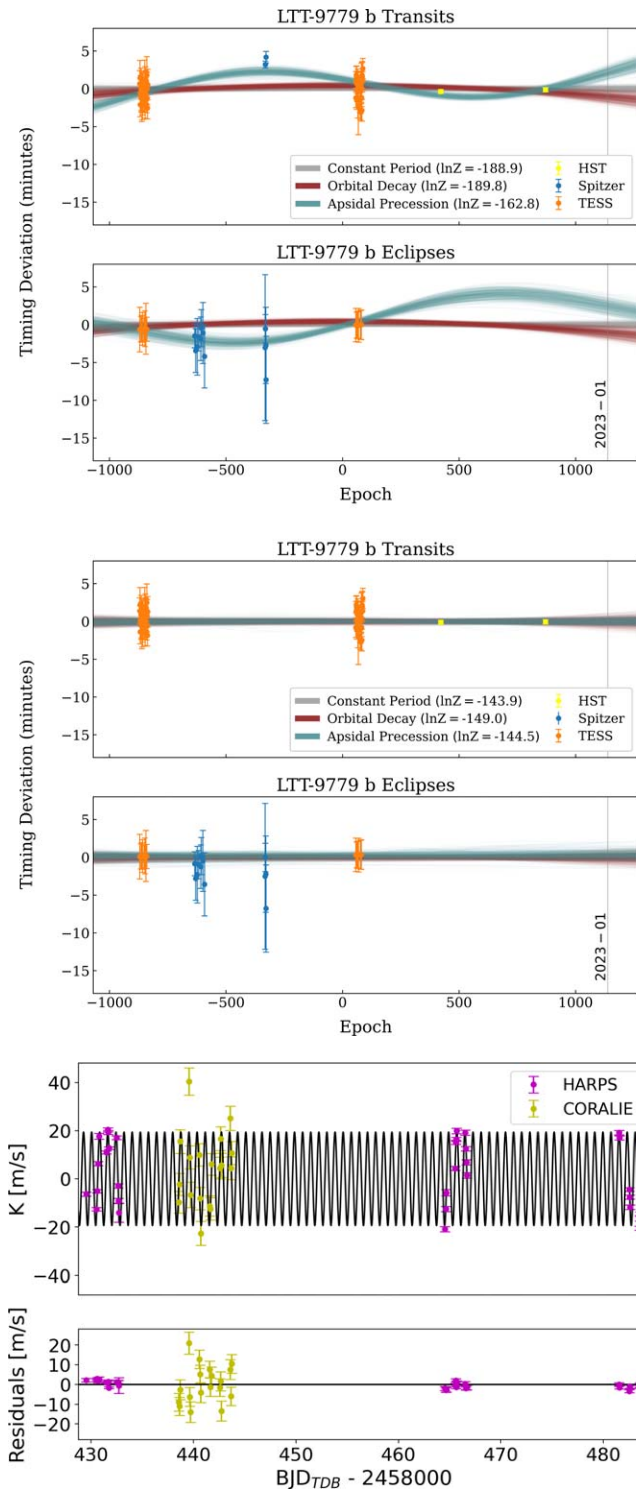


**Figure 11.** Plots from our ephemeris fitting for LTT 9779 b. Top: observed minus calculated ( $O - C$ ) plots for all transit and eclipse midtimes. The reference epoch is set to be halfway between the first and last transit used in this work. Traces from all three models, linear (gray), decay (red), and precession (turquoise), are also shown. Middle:  $O - C$  plots once the Spitzer transits have been discarded. In doing so, all evidence for nonlinear ephemerides is also removed. Bottom: fit to the literature radial velocity data. For brevity, we only show the best-fit model to this data when considering a constant period and when the Spitzer transit midtimes have been discarded, which we adopt as our favored model. However, these data are used in all our fits.

apsidal precession model, however, is highly favored with a Bayesian evidence of  $\ln(E) = -201.2$ . Examination of the data shows that the Spitzer transits have significant observed minus calculated ( $O - C$ ) residuals compared to the uncertainties on the midtime (see Figure 11). These were taken from fits conducted by Crossfield et al. (2020) to the phase curves of LTT 9779 b. The eclipse midtimes from these phase curves (which were taken from the same data but independently fitted by Dragomir et al. 2020) do not show, in contrast, the same magnitude of deviation, thereby suggesting these points may be outliers rather than an actual detection of a significant deviation from the expected time.

Due to the shape of the decay and precession models within an  $O - C$  plot (i.e., a parabola and a sine curve), we surmise that these Spitzer transit midtimes could be driving the model toward a solution that favors precession, with the large gaps in the transit coverage also enabling such a solution. Therefore, we also explore fits to the data without the Spitzer transit midtimes. In this case, the linear model is preferred with  $\ln(E) = -181.0$  versus  $\ln(E) = -185.8$  and  $\ln(E) = -181.7$  for the orbital decay and apsidal precession models, respectively. Though the evidence against apsidal precession versus a linear ephemeris is only marginal, the best-fit solution for the precession model is linear within the uncertainties (see Table 6). The inclusion or exclusion of the Spitzer transit midtimes has a minimal impact on the best-fit linear period but, given the potentially spurious nature of the midtimes, we report the recovered period without these points in Table 2. For completeness, the best-fit parameters for all fits are given in the Appendix.

## 4. Discussion

### 4.1. The Atmosphere of LTT 9779 b

We have presented transmission observations of the hot Neptune LTT 9779 b, extracting a spectrum from 0.8–1.6  $\mu\text{m}$ . Our best-fit free chemistry model shows evidence for high abundances of  $\text{H}_2\text{O}$  and  $\text{CO}_2$ . To test the strength of each of these detections, we run additional retrievals. Without  $\text{H}_2\text{O}$  in the model, the best-fit model provides a worse fit to the data with the Bayesian evidence suggesting that the presence of  $\text{H}_2\text{O}$  is preferred by  $3.12\sigma$ . In this model without  $\text{H}_2\text{O}$ , the retrieved  $\text{CO}_2$  abundance is even higher than in our preferred model as shown in Figure 12. We also run a retrieval without  $\text{CO}_2$ , finding that the Bayesian evidence was reduced in this case: the inclusion of  $\text{CO}_2$  was preferred by  $2.01\sigma$ . The lower significance of this detection is likely due to the fact that WFC3 data only have limited sensitivity to carbon-bearing species. Furthermore, it has been shown that carbon-bearing species identified within a preferred model can be dependent upon how the retrieval is set up (e.g., Changeat et al. 2020). Interestingly, the removal of  $\text{CO}_2$  from the model does not lead to the detection of  $\text{CO}$  or  $\text{HCN}$ . Instead, the  $\text{H}_2\text{O}$  abundance is affected with a slightly higher volume mixing ratio being preferred (see Figure 12). The other molecular species that was constrained in the free chemistry case was  $\text{FeH}$  and we found that our retrievals preferred its presence by  $2.13\sigma$ . Hence, for all these species we find a relatively weak detection significance.

**Table 2**  
Stellar and Planetary Parameters Used or Derived in This Study

Parameter	Unit	Value	Source
$R_*$	$R_\odot$	$0.949 \pm 0.006$	J20
$M_*$	$M_\odot$	$1.02^{+0.02}_{-0.03}$	J20
$T_*$	K	$5480 \pm 42$	J20
$\log(g)$	$\log_{10}(\text{cm s}^{-2})$	$4.47 \pm 0.11$	J20
Fe/H	dex	$0.25 \pm 0.04$	J20
Age	Gyr	$2.0^{+1.3}_{-0.9}$	J20
$P_{\text{rot}}$	days	$<45$	J20
$R_p$	$R_\oplus$	$4.72 \pm 0.23$	J20
$M_p$	$M_\oplus$	$29.32^{+0.78}_{-0.81}$	J20
$a/R_*$		$3.877^{+0.090}_{-0.091}$	J20
$i$	degrees	$76.39 \pm 0.43$	J20
$e$		$<0.058$	J20
$T_{\text{eq}}$	K	$1978 \pm 19$	J20
$T_0$	BJD <sub>TDB</sub>	$2,459,043.310602 \pm 0.000090$	TW
$P$	days	$0.79206410 \pm 0.00000014$	TW

**Note.** J20: Jenkins et al. (2020); TW: this work.

Our retrievals with ASTeRA prefer models with a high spot coverage. Such coverages are unrealistic, but could potentially be caused by assuming the wrong star temperature in our models. As the spots in the model are hotter than the rest of the stellar surface, the unrealistic coverage might indicate that our assumed stellar temperature is too low. We explore this possibility by independently determining the basic stellar parameters. We perform an analysis of the broadband spectral energy distribution (SED) of the star together with the Gaia DR3 parallax (with no systematic offset applied; see, e.g., Stassun & Torres 2021), in order to determine an empirical measurement of the stellar radius, following the procedures described in Stassun & Torres (2016) and Stassun et al. (2017, 2018). We pull the  $B_T V_T$  magnitudes from Tycho-2, the JHK<sub>S</sub> magnitudes from the Two Micron All Sky Survey (2MASS), the W1–W4 magnitudes from the Wide-field Infrared Survey Explorer (WISE), the  $G_{\text{BP}}G_{\text{RP}}$  magnitudes from Gaia, as well as the NUV flux from the Galaxy Evolution Explorer (GALEX). Together, the available photometry spans the full stellar SED over the wavelength range 0.2–20  $\mu\text{m}$  (see Figure 13).

We perform a fit using PHOENIX stellar atmosphere models, with the free parameters being the effective temperature ( $T_{\text{eff}}$ ) and metallicity ([Fe/H]); we set the extinction  $A_V \equiv 0$ , due to the close proximity of the system, and we assume a surface gravity  $\log g \approx 4.5$  as appropriate for a main-sequence dwarf. Finally, we use the Gaia spectrum as a consistency check for the overall absolute flux calibration.

The resulting fit (Figure 13) has a best-fit  $T_{\text{eff}} = 5450 \pm 75$  K and [Fe/H] =  $0.0 \pm 0.3$ , with a reduced  $\chi^2$  of 1.4. Integrating the model SED gives the bolometric flux at Earth,  $F_{\text{bol}} = 3.503 \pm 0.041 \times 10^{-9}$  erg s<sup>-1</sup> cm<sup>-2</sup>. Taking the  $F_{\text{bol}}$  together with the Gaia parallax directly gives the bolometric luminosity,  $L_{\text{bol}} = 0.7173 \pm 0.0084 L_\odot$ , which with the  $T_{\text{eff}}$  gives the stellar radius,  $R_* = 0.951 \pm 0.018 R_\odot$ . In addition, we can estimate the stellar mass from the empirical eclipsing-binary-based relations of Torres et al. (2010), giving  $M_* = 0.96 \pm 0.06 M_\odot$ . Finally, the mass and radius together give the mean stellar density,  $\rho_* = 1.58 \pm 0.13$  g cm<sup>-3</sup>.

These values are consistent with those from Jenkins et al. (2020), which we use for all the analyses here. In particular, the

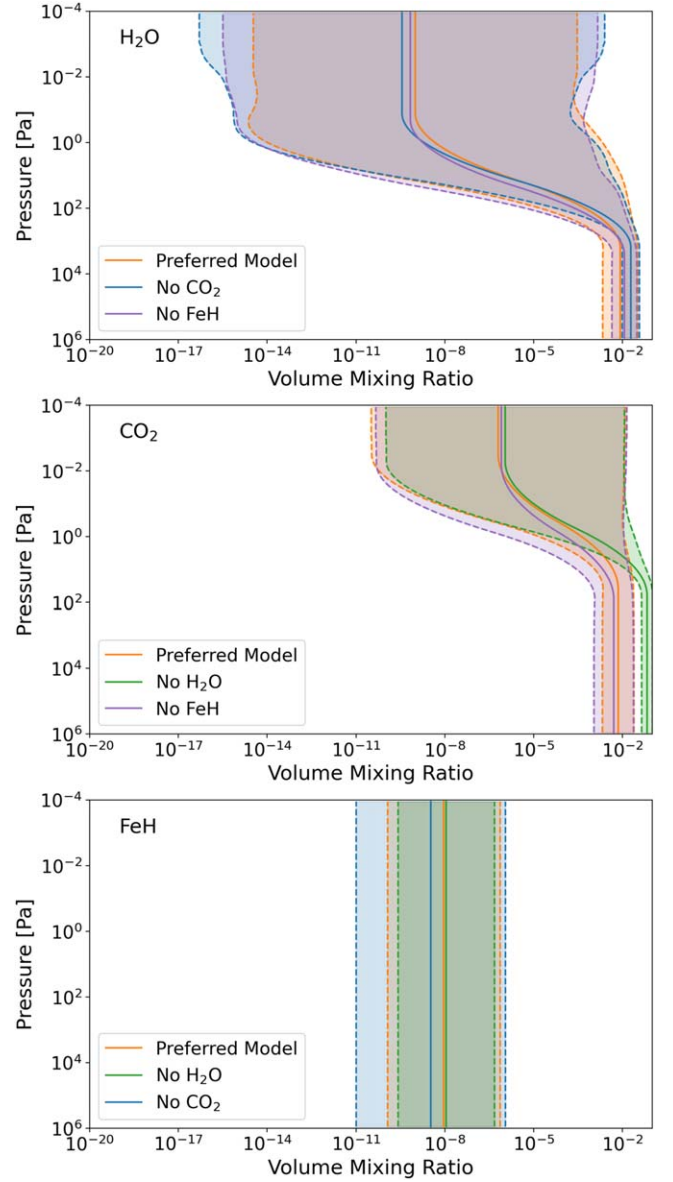


**Figure 12.** Changes to the retrieved abundances of H<sub>2</sub>O, CO<sub>2</sub>, and FeH when one of the other molecules is removed from the retrieval. In all three cases, the model without the molecule is not preferred to the full setup. Comparing the Bayesian evidence suggests the presence of H<sub>2</sub>O is preferred by 3.11 $\sigma$  while there is a 2.35 $\sigma$  preference for the inclusion of CO<sub>2</sub> and a 2.12 $\sigma$  preference for FeH. All these retrievals were conducted with an isothermal temperature–pressure profile.

recovered temperature is not higher than assumed: it is, in fact, slightly lower ( $T_{\text{eff}} = 5450 \pm 75$  K versus  $5480 \pm 42$  K). Therefore, it seems that this is not the cause of the high spot coverage preferred in our retrievals with ASTeRA.

Given its high irradiation, it was anticipated that LTT 9779 b would be undergoing significant mass loss. Hence, it might be expected that this escape could be observed using tracers of atmospheric escape such as the helium triplet at 1.083  $\mu\text{m}$  and thus that the nondetection within the HST WFC3 G102 is surprising. However, it is important to consider that the observability of the atmospheric escape via this particular tracer is not only dependent on the level of atmospheric escape. The population of helium in the triplet state also plays a critical role and this has been shown to depend on the nature of the stellar irradiance. The triplet state is more readily populated for

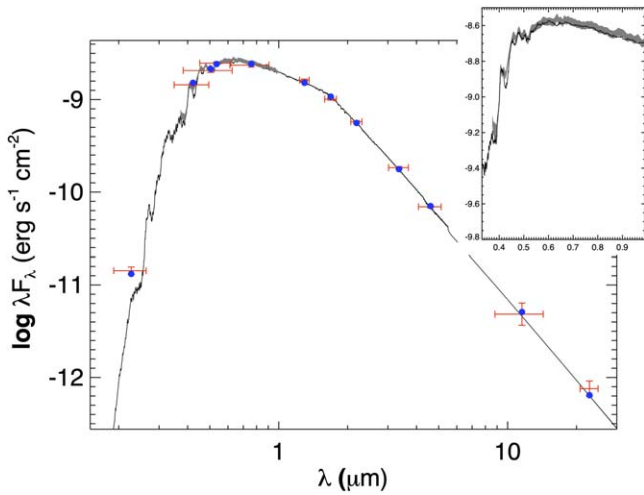


**Figure 13.** SED of LTT 9779. Red symbols represent the observed photometric measurements, where the horizontal bars represent the effective width of the passband. Blue symbols are the model fluxes from the best-fit PHOENIX atmosphere model (black). The Gaia spectrum is also shown as a gray swathe; the inset plot shows a close up.

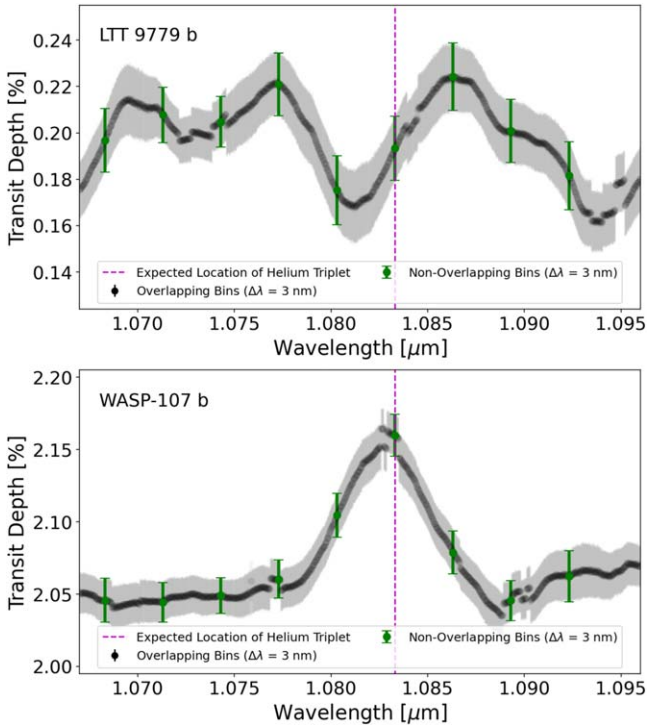


**Figure 14.** High-resolution ( $\delta\lambda = 30 \text{ \AA}$ , spaced by  $0.1 \text{ \AA}$ ) HST WFC3 G102 data for LTT 9779 b (top) and WASP-107 b (bottom). In the latter case, the excess absorption due to the helium triplet is clearly apparent.

K-dwarf hosts with their relatively low mid-UV flux (which can photoionize helium out of the triplet state) to EUV flux (which is both a significant contributor to driving the escape itself and populating the triplet via recombinations) compared to warmer G-type stars (Oklopčić 2019). Our work shows that LTT 9779 b indeed receives a high mid-UV flux, with our model finding that mid-UV photoionizations are the main depopulating source for triplet-state helium and hence largely responsible for the lack of a clear detection of helium at  $1.083 \mu\text{m}$ . To cement this nondetection further, we apply the same fitting procedure to the HST WFC3 G102 data of

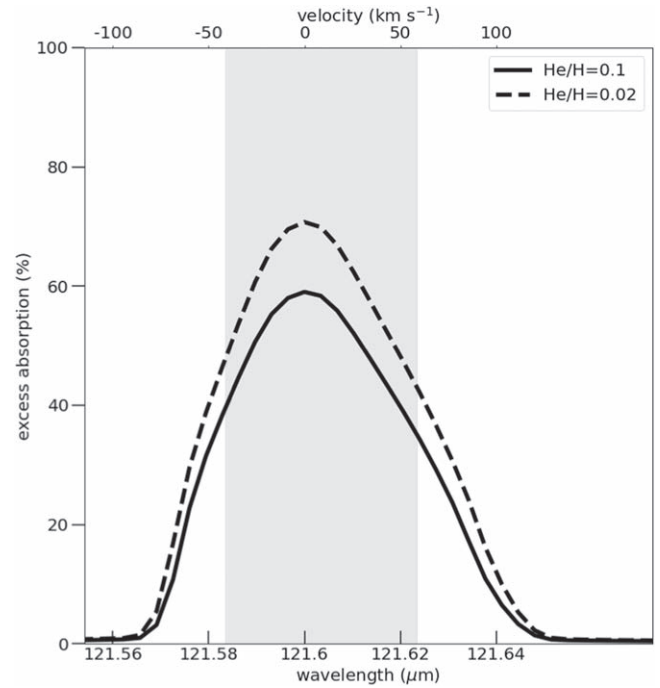


**Figure 15.** Anticipated  $\text{Ly}\alpha$  signature for LTT 9779 b assuming 2/98 He/H (dotted) and 10/90 He/H (solid). While no trace of atmospheric escape was found with the helium triplet, this tracer may offer another chance to detect and/or constrain the escape rate of LTT 9779 b’s atmosphere.

WASP-107 b, which is shown in Figure 14 and highlight the strength of the signal seen in that case.

Alternative tracers, such as the commonly used hydrogen  $\text{Ly}\alpha$  line may allow the predicted strong escape of LTT 9779 b to be observed. Again utilizing the model of Allan & Vidotto (2019), we predict significant absorption in the uncontaminated  $\text{Ly}\alpha$  line wings and show the resulting profile in Figure 15. However, we note that three-dimensional modeling considering the interaction with the stellar wind is required for a realistic  $\text{Ly}\alpha$  prediction, given that high-velocity blueshifted absorption originates due to interaction with the stellar wind (Carolan et al. 2021). We leave such a detailed analysis for further work.

In their study of helium escape for planets close to the Neptune desert, Vissapragada et al. (2022) derived a boundary below which a planet could not have lost more than 50% of its initial mass to photoevaporation. As LTT 9779 b is situated below this region, they noted that it was unlikely to be the photoevaporated core of a giant gaseous planet, with high-eccentricity orbital migration being the more likely explanation for the planet’s current characteristics as the planet could have been delivered to its current location relatively late. Further evidence for this could be present in the planet’s atmospheric composition (e.g., a high C/O ratio) or via the detection of a remaining eccentricity  $i$  the orbit of LTT 9779 b. However, the data analyzed here, and in previous studies (e.g., Crossfield et al. 2020; Dragomir et al. 2020), are not able to provide such evidence.

Hence, it is hard to conclude a great deal about the nature of the atmosphere of LTT 9779 b. We expect that far better constraints on the nature of LTT 9779 b’s atmosphere from JWST NIRISS (Doyon et al. 2012) phase-curve observations, which have already been taken as part of Cycle 1. The transit portion of the JWST phase curve may also shed light on spectral variability when compared to the data presented here.

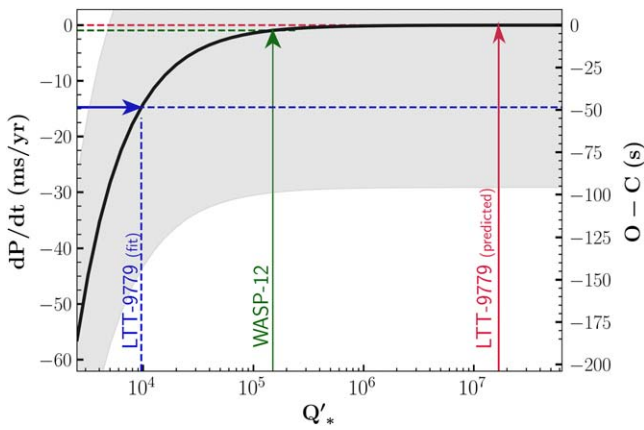


**Figure 16.** The orbital period derivative in milliseconds per year expected for LTT 9779 b given different values of the modified stellar tidal quality factor  $Q'_*$ . The right-hand vertical axis shows the expected  $O - C$  signal over the current observational baseline and the gray shaded region represents the average timing uncertainty of the data. Three values of  $Q'_*$  are highlighted: (1) derived with Equation (11) from the best-fit orbital decay rate when the Spitzer transit timings were included, (2) predicted with Equation (13) from the tidal forcing period of the system, and (3) the value for WASP-12 from Wong et al. (2022).

Given the wider spectral coverage and higher S/N, the NIRISS transmission data should also be able to disentangle atmospheric features more easily from stellar contamination. An analysis of the global temperature and chemistry will test the implications made in this study, and those from the Spitzer data, and provide a more accurate interpretation of both. While we do not detect the signature of atmospheric escape from the helium triplet in this work, the JWST NIRISS observations may provide a detection. Additionally, observations with HST of the Ly $\alpha$  line may provide better constraints on the current escape rate of LTT 9779 b's atmosphere and thus on the nature of the hot-Neptune desert.

Furthermore, eclipse observations of LTT 9779 b with CHEOPS have found evidence for variability (AO2-013; PI: James Jenkins), with additional observations being taken to confirm this (AO3-022; PI: James Jenkins). HST WFC3 UVIS is also being used to study the eclipse spectrum of LTT 9779 b (GO-16915; PI: Michael Radica; Radica et al. 2022) and these data may further constrain the eclipse-depth variability as well as helping to determine the albedo. Given the HST observations used here were taken roughly a year apart, the conclusions of these eclipse studies may indicate that, while the G102 and G141 data have similar transit depths in their overlapping spectral regions, dynamic changes to the planet may mean the spectra are not compatible.

#### 4.2. The Orbit of LTT 9779 b

While we do not find compelling evidence in the data to suggest that LTT 9779 b is undergoing orbital decay, we explore the magnitude of tidal dissipation of energy within the star necessary to yield an observable signal. Assuming the constant-phase lag model for tidal evolution suggested by Goldreich & Soter (1966), the expected decay rate is given by:

$$\frac{dP}{dt} = -\frac{27\pi}{2Q'_*} \left(\frac{M_p}{M_*}\right) \left(\frac{R_*}{a}\right)^5, \quad (11)$$

where  $M_p$  is the planet's mass,  $M_*$  is the star's mass,  $R_*$  is the star's radius,  $a$  is the semimajor axis of the planet's orbit, and

$Q'_*$  is the modified tidal quality factor. From our fit of the orbital decay model this yields a  $Q'_*$  of  $1.5 \times 10^4$  (without Spitzer transits) or  $2.1 \times 10^3$  (with Spitzer transits), both far outside the range of  $10^5 < Q'_* < 10^8$  expected given the current theory of energy dissipation within the convective envelopes of cool stars (Penev et al. 2018) and two orders of magnitude smaller than the value of  $1.5 \times 10^5$  derived for WASP-12 (Patra et al. 2017; Yee et al. 2019; Wong et al. 2022). Based on this analysis and the strong preference of the Bayes factor for a linear ephemeris, we conclude that the best-fit orbital decay rates from the data do not warrant further consideration.

Penev et al. (2018) derived an empirical model for  $Q'_*$  given the tidal forcing period of the star–planet system  $P_{\text{tide}}$  from an analysis of all known exoplanet systems with  $M_p > 0.1 M_{\text{Jup}}$ ,  $P < 3.5$  days, and  $T_{\text{eff},*} < 6100$  K, the parameter space in which the LTT 9779 system resides. They found:

$$Q'_* = \max \left[ \frac{10^6}{(P_{\text{tide}}/\text{days})^{3.1}}, 10^5 \right] \text{ where} \quad (12)$$

$$P_{\text{tide}} = 1/2 \left( \frac{1}{P_{\text{orb}}} - \frac{1}{P_{\text{spin}}} \right). \quad (13)$$

Based on this result, we predict  $Q'_*$  for LTT 9779 by adopting a stellar rotation period of 45 days, as found in Jenkins et al. (2020). Taking this rotation period at face value requires the assumption that the orbit of LTT 9779 b is aligned with the stellar rotation axis and so this is, in effect, an upper limit. With this model and assumption, we predict that  $Q'_* = 1.7 \times 10^7$  for LTT 9779, which corresponds to an orbital decay rate of  $-0.0085 \text{ ms yr}^{-1}$  for LTT 9779 b. Figure 16 shows that if orbital decay were occurring at this rate, the  $O - C$  expected within the current observational baseline would be far below the average uncertainty of the midtransit times. In the near future, more data will be available from CHEOPS, HST, JWST, and TESS observations. By the time the next TESS data for this planet are taken in Sector 69, LTT 9779 b will have orbited its host star around 2300 times since the first detection of a transit. If we assume the  $Q'_*$  predicted from the tidal forcing period, the  $O - C$  would be a mere  $-0.05$  s by that time. Thus, despite the very short orbital period of LTT 9779 b it is unlikely that, if occurring, tidal orbital decay could be detected.

Likewise, our fit to the timing data suggests that there is only evidence for orbital precession when the Spitzer data are included and that the best-fit apsidal precession model seems to be exploiting the large gaps in the coverage of the transit and eclipse data. Nevertheless, we explore the potential magnitude of precession we might expect for this world, comparing it to preferred value from our fit. We estimate a maximum theoretical apsidal precession rate by summing the contributions of general relativistic effects and tidal and rotational bulges of both the planet and star, using Equations (6), (10), and (12) from Ragozzine & Wolf (2009). The magnitude of apsidal precession raised by tidal and rotational bulges depends on the Love number  $k_2$  of the perturbing body, thus we assume a value of  $k_{2,*} = 0.03$  for LTT 9779, typical of Sun-like main-sequence stars (Ragozzine & Wolf 2009), and  $k_{2,p} = 0.3$  for LTT 9779 b. We chose the latter as a generous value for a hot Neptune with a core mass fraction of  $\sim 0.9$  (Jenkins et al. 2020) given the results of the case study of the hot Neptune GJ 436 b

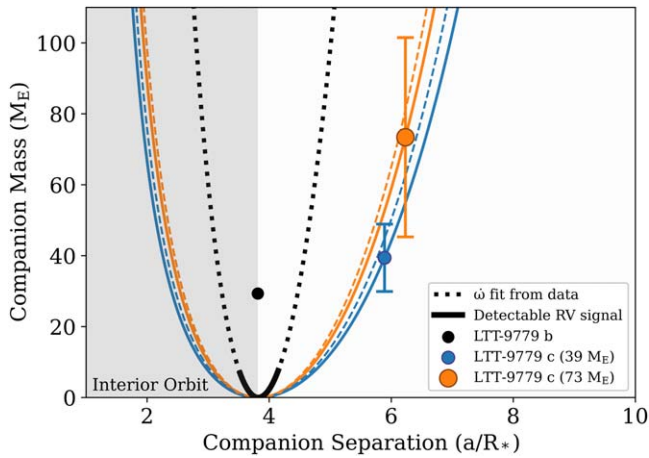


**Figure 17.** One source of orbital precession could be other planets within the system. We show the possible parameter space for the mass and orbital separation of a companion planet (LTT 9779 c) for three possible precession rates: the best-fit value from our model fit (black) and those of the two candidate solutions identified in Pearson (2019; blue and orange). The blue and orange dashed lines are the same as the latter but corrected for the expected precession from other effects calculated in Equation (14). The solid part of the black line represents the possible mass-separation solutions for a companion planet that would provide the best-fit apsidal precession rate from the timing data while remaining undetected in the radial velocity data ( $K < 5 \text{ m s}^{-1}$ ) given the residuals of our fit (see Figure 11).

by Kramm et al. (2011), noting that lower values would reduce the predicted rates of precession. Given that we additionally assume the upper limit of orbital eccentricity ( $e < 0.058$ ) from Jenkins et al. (2020), we effectively calculate the maximum possible precession rate from the aforementioned effects. Our calculations yield:

$$\begin{aligned} \dot{\omega}_{\text{tot}} &= \dot{\omega}_{\text{tide},p} + \dot{\omega}_{\text{tide},*} + \dot{\omega}_{\text{rot},p} + \dot{\omega}_{\text{rot},*} + \dot{\omega}_{\text{GR}} \\ &= (4.0 \times 10^{-5} + 1.5 \times 10^{-7} + 2.6 \times 10^{-6} \\ &\quad + 3.6 \times 10^{-8} + 1.1 \times 10^{-5}) \text{ rad}/E \\ &\approx 5.4 \times 10^{-5} \text{ rad}/E, \end{aligned} \quad (14)$$

where  $\dot{\omega}_{\text{tide}}$  and  $\dot{\omega}_{\text{rot}}$  refer to the contribution from the tidal and rotational bulges, respectively, and  $\dot{\omega}_{\text{GR}}$  is from general relativistic effects. The cumulative precession rate of  $5.4 \times 10^{-5} \text{ rad}/E$  is two orders of magnitude below our best-fit model ( $d\omega/dE = 3.1 \times 10^{-3} \text{ rad}/E$ ). Given that we have assumed characteristics that would maximize the theoretical apsidal precession rate, we conclude that none of the above effects could be the source of the timing variation seen in Figure 11.

We also consider the possibility that apsidal precession may be induced by an additional body within the system. Before the confirmation of LTT 9779 b by Jenkins et al. (2020), there were suggestions of other planets within the LTT 9779 system (Pearson 2019), the best solutions being a  $39.4 \pm 9.5 M_{\oplus}$  planet on a 1.516 day orbit and a  $73.4 \pm 28.1 M_{\oplus}$  planet on a 1.65 day orbit. Using Equation (8) from Heyl & Gladman (2007), we calculate the expected apsidal precession rate raised by these proposed companions. However, we again find that the predicted precession rate(s) would be far below the best-fit value from our timing models (see Figure 17), and note that any companion inducing such a strong precession rate would be easily detectable in the radial velocity data. Hence, we find no reasonable way to explain the precession rate fit when

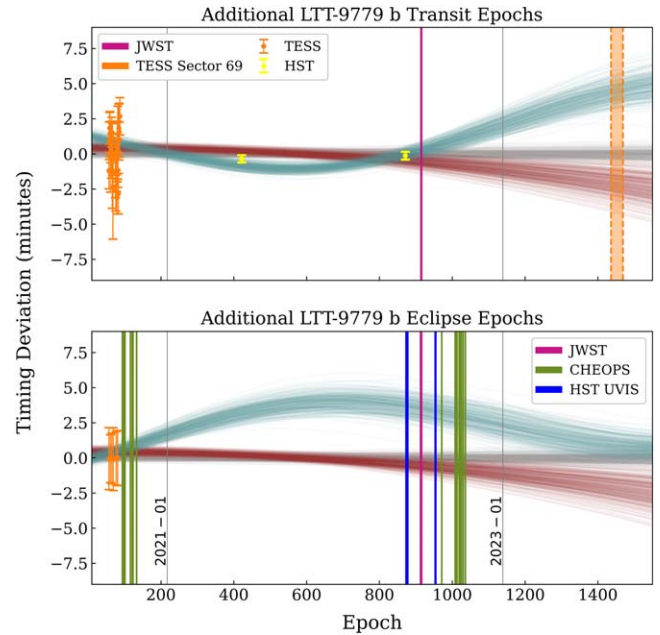


**Figure 18.** Epochs covered by existing data with CHEOPS, JWST, and HST WFC3 UVIS, as well as that will be covered in TESS Sector 69. Overplotted are our best-fit models when the Spitzer transit timings are included in the analysis. With these data, the apsidal precession model is likely to be conclusively ruled out while the decay model will be harder to distinguish from the linear period, although stronger constraints on the maximum decay rate could be placed.

including the Spitzer transits, concluding that it is not a viable orbital solution and that it is likely due to poor sampling of the transit and eclipse epochs since the discovery of LTT 9779 b. The combination of current and future transit and eclipse data from CHEOPS, HST WFC3 UVIS, JWST, and TESS should be capable of providing definitive evidence against the precession model, as highlighted in Figure 18.

## 5. Conclusions

We use open-source codes to reduce and analyze the HST WFC3 G102 and G141 transmission spectrum of the ultrahot Neptune LTT 9779 b. However, the constraints placed on the atmospheric parameters from these data are poor, with the best-fit value of many parameters sometimes simply being the center of the prior. Nevertheless, our retrievals on these data prefer the presence of  $\text{H}_2\text{O}$ ,  $\text{CO}_2$ , and FeH and the significance of these detections varies from  $2\text{--}3\sigma$ . On the other hand, the best-fit values for the molecular abundances are higher than expected from chemical equilibrium models. While we find no evidence for excess absorption around the helium triplet, our modeling shows this is expected given the stellar irradiation. We find little evidence to suggest that LTT 9779 b's orbit is decaying, but this is unsurprising given the expected magnitude of the orbital decay and its small effect on the transit times. While a model for apsidal precession can preferably fit the timing data, it yields a solution which cannot be physically explained and the detection hinges purely on two transit timings from Spitzer. Therefore, while these HST data shed further light on the nature of LTT 9779 b, much remains to be discovered and many questions are left unanswered. Analysis of data from CHEOPS, HST WFC3 UVIS, and JWST NIRISS should begin to resolve some of these outstanding queries to help us understand this rare and intriguing world.

### Acknowledgments

B.E. is grateful to Wilson Joy Skipper for coordinating the HST program GO-16457, under which these HST WFC3 observations were acquired. Q.C. is funded by the European Space Agency under the 2022 ESA Research Fellowship Program. We acknowledge support from ESA through the Science Faculty—Funding reference ESA-SCI-SC-LE-117. N. S. acknowledges support from the PSL Iris-OCAV project, and from NASA (Grant #80NSSC19K0336). This project has also received funding from the European Research Council (ERC) under the European Union’s Horizon 2020 research and innovation program (grant agreements No. 758892, ExoAI, and No. 817540, ASTROFLOW) and from the Science and Technology Funding Council (STFC) grant ST/S002634/1 and ST/T001836/1 and from the UK Space Agency grant ST/W00254X/1.

### Data Availability

This work is based upon publicly available observations taken with the NASA/ESA Hubble Space Telescope as part of proposals GO-16457 (PI: Billy Edwards; Edwards et al. 2020a) and GO-16166 (PI: Kevin France; France et al. 2020). These observations were facilitated by the Space Telescope Science Institute, which is operated by the Association of Universities for Research in Astronomy, Inc., under NASA contract NAS 5-26555. The data were obtained from the Mikulski Archive for Space Telescopes (MAST) at the Space Telescope Science Institute. The specific observations analyzed can be accessed via doi:[10.17909/dr7t-g194](https://doi.org/10.17909/dr7t-g194). We are thankful to those who operate the Hubble Space Telescope and the corresponding

archive, the public nature of which increases scientific productivity and accessibility (Peek et al. 2019).

*Software:* Iraclis (Tsiaras et al. 2016c), TauREx3 (Al-Refaie et al. 2021), TauREx GGChem (Woitke et al. 2018; Al-Refaie et al. 2022), ASteRA (Thompson et al. 2023), ExoTETHyS (Morello et al. 2020), PyLightcurve (Tsiaras et al. 2016b), RadVel (Fulton et al. 2018), Multinest (Feroz et al. 2009; Buchner et al. 2014), Astropy (Astropy Collaboration et al. 2018), h5py (Collette 2013), emcee (Foreman-Mackey et al. 2013), Matplotlib (Hunter 2007), Pandas (McKinney 2011), Numpy (Oliphant 2006), SciPy (Virtanen et al. 2020), and corner (Foreman-Mackey 2016).

### Appendix

Here, we provide the posteriors for several of the retrievals conducted in this study. Figure 19 shows the posteriors for our preferred free chemistry retrieval while the free chemistry retrieval with an offset between the HST WFC3 G102 and G141 data sets is shown in Figure 20. Likewise, Figures 21 and 22 show the posteriors from the chemical equilibrium retrievals with and without an offset, respectively. Finally, in Figure 23 we shown the posteriors from our retrieval which included the effects of spots and faculae.

Table 2 gives the stellar and planetary parameters used in this study while the HST WFC3 G102 and G141 spectra are given in Table 3. We also provide the transit and eclipse midtimes used in this study in Tables 4 and 5, respectively. We also provide the best-fit parameters from the linear, decay, and precession models in Table 6.

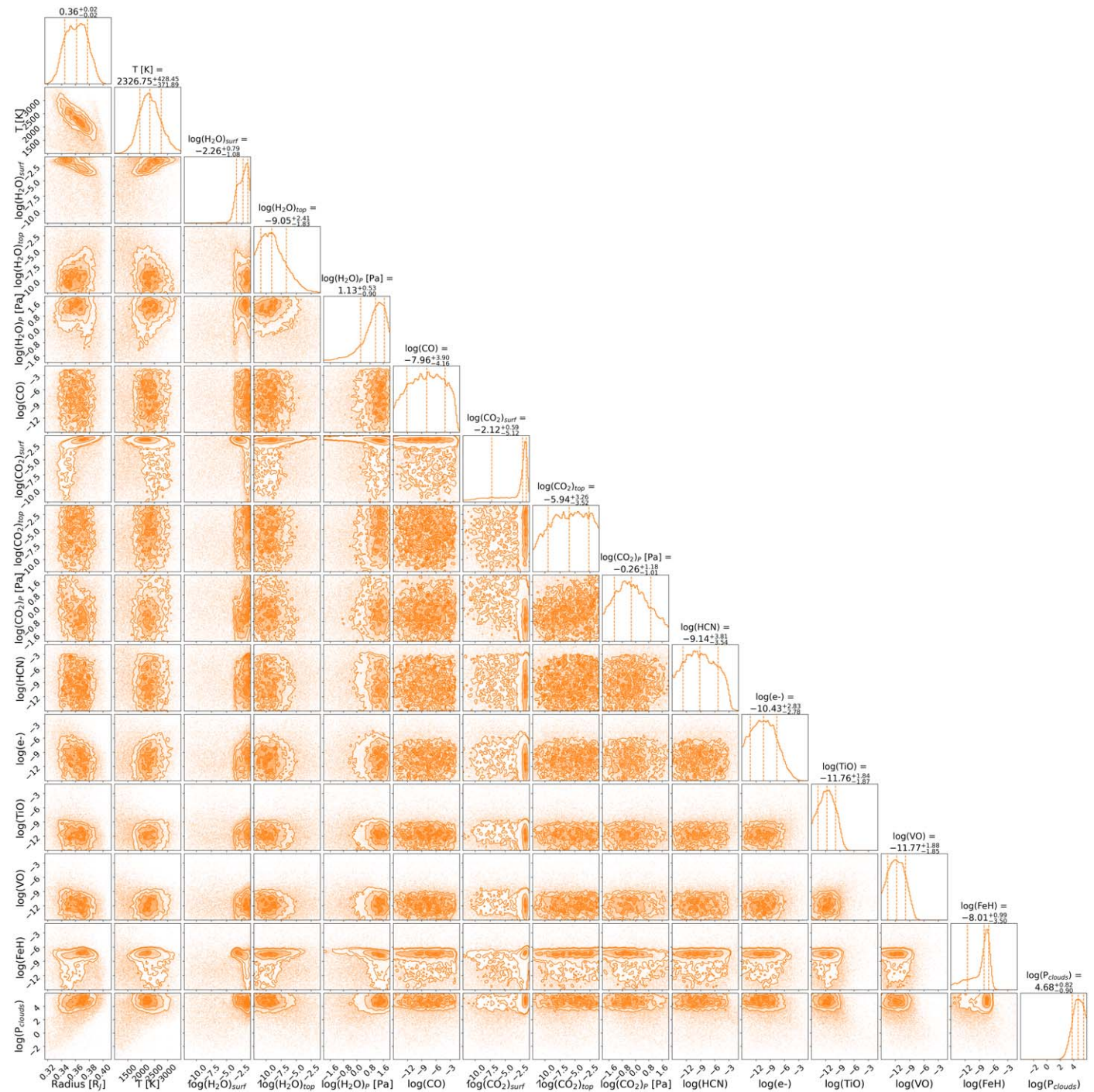


**Figure 19.** Posterior distributions for our preferred free chemistry retrieval which included an isothermal temperature profile and two-layer abundances for H<sub>2</sub>O and CO<sub>2</sub>. We note that, for many parameters, the best-fit value is simply the mean of the prior.

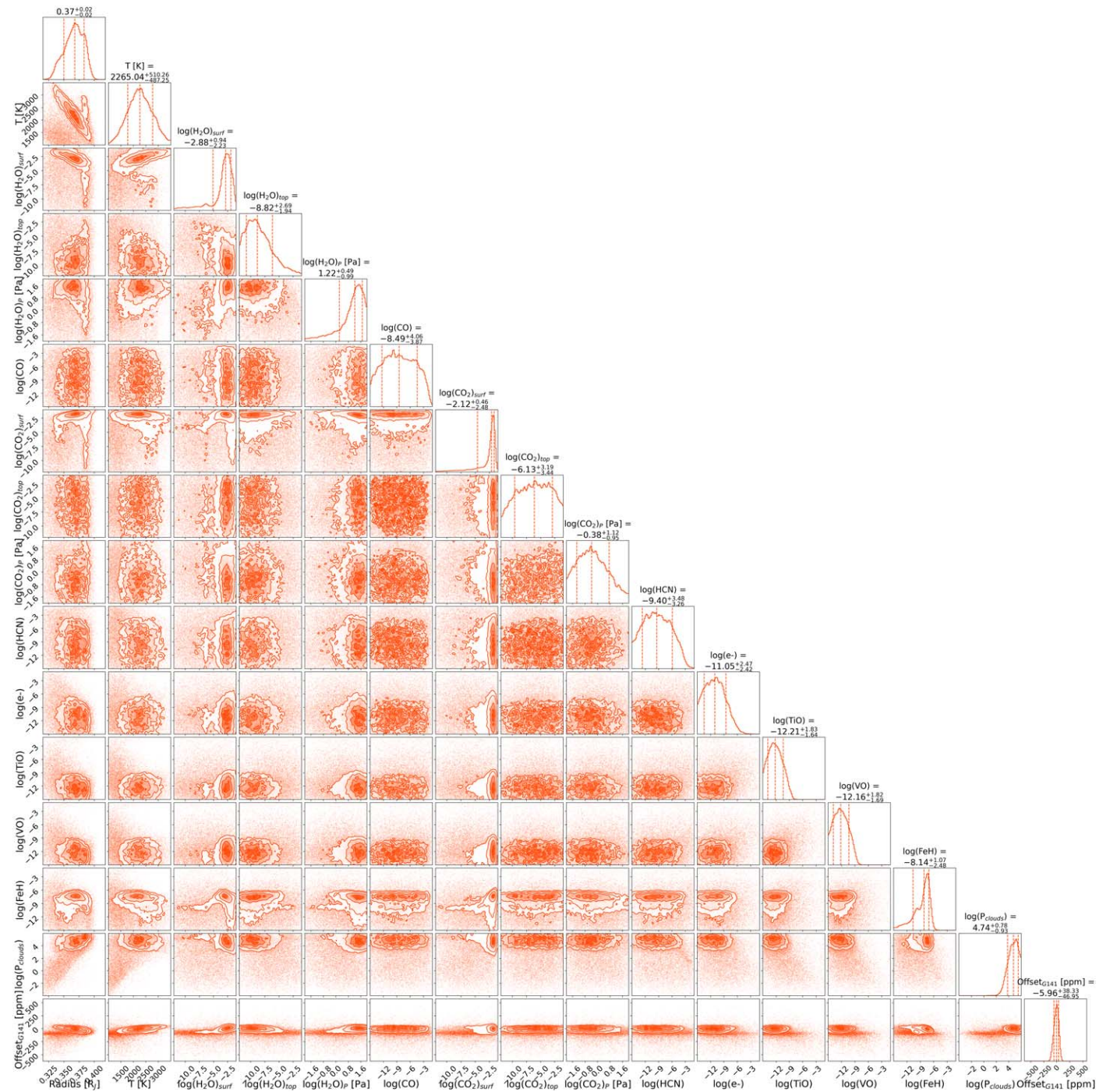


**Figure 20.** Posterior distributions for the free chemistry retrieval which included an offset in the HST WFC3 G141 data. The retrieval converges to a solution which has a slight offset, but the “no offset” solution is well within the 1σ uncertainties. Furthermore, the Bayesian evidence for this retrieval is significantly less than that of the same retrieval minus an offset parameter. The difference in the Bayesian evidence suggests an offset between the data sets is rejected at the 3.7σ level.

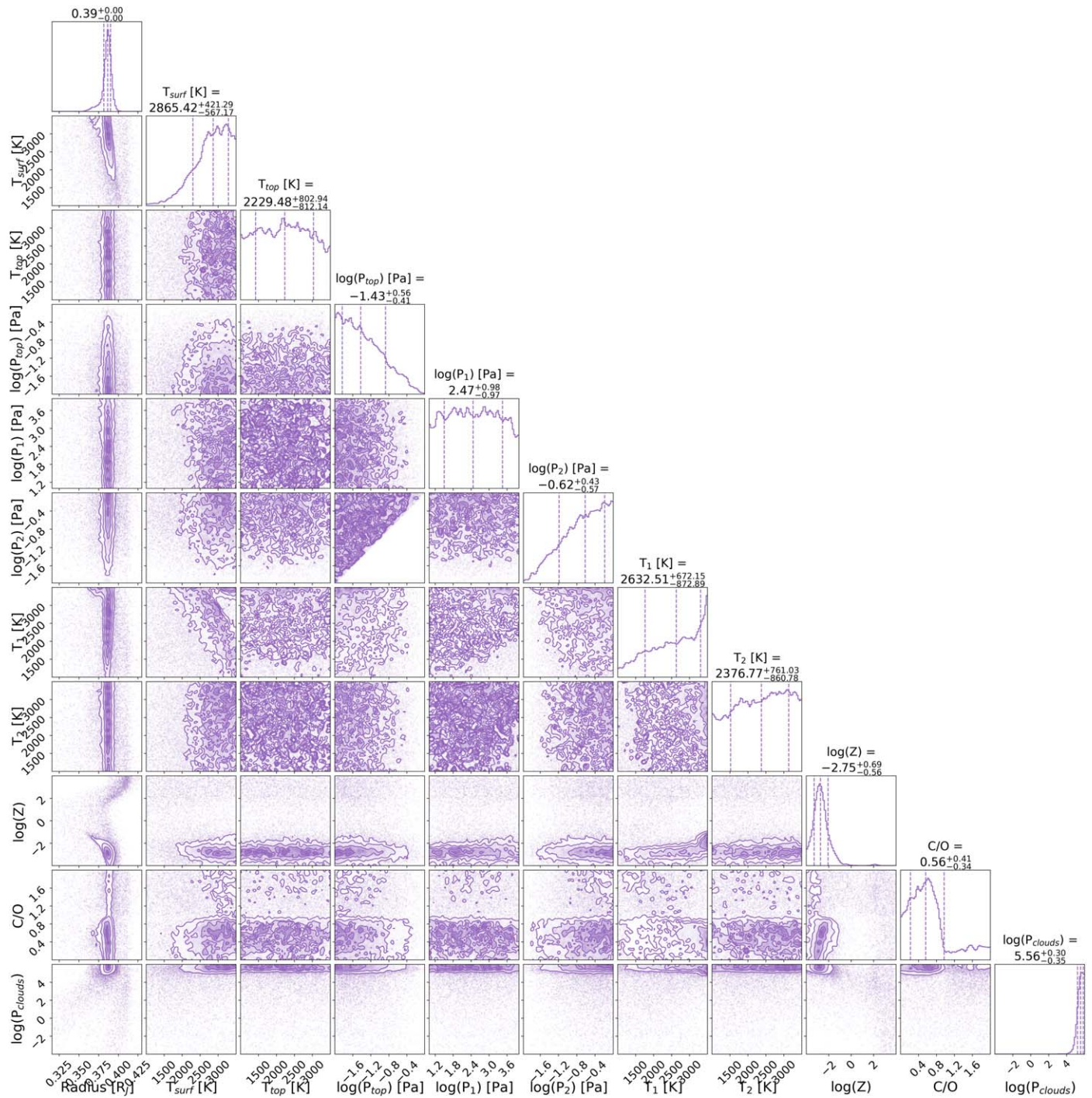


**Figure 21.** Posterior distributions for our preferred chemical equilibrium retrieval which included a nonisothermal temperature profile. We note that this retrieval was not preferred over the free chemistry model given in Figure 19, with the Bayesian evidence preferring the latter to  $2.4\sigma$ . Additionally, while the nonisothermal temperature profile led to a preferable fit, it did not lead to a well-constrained temperature–pressure profile.

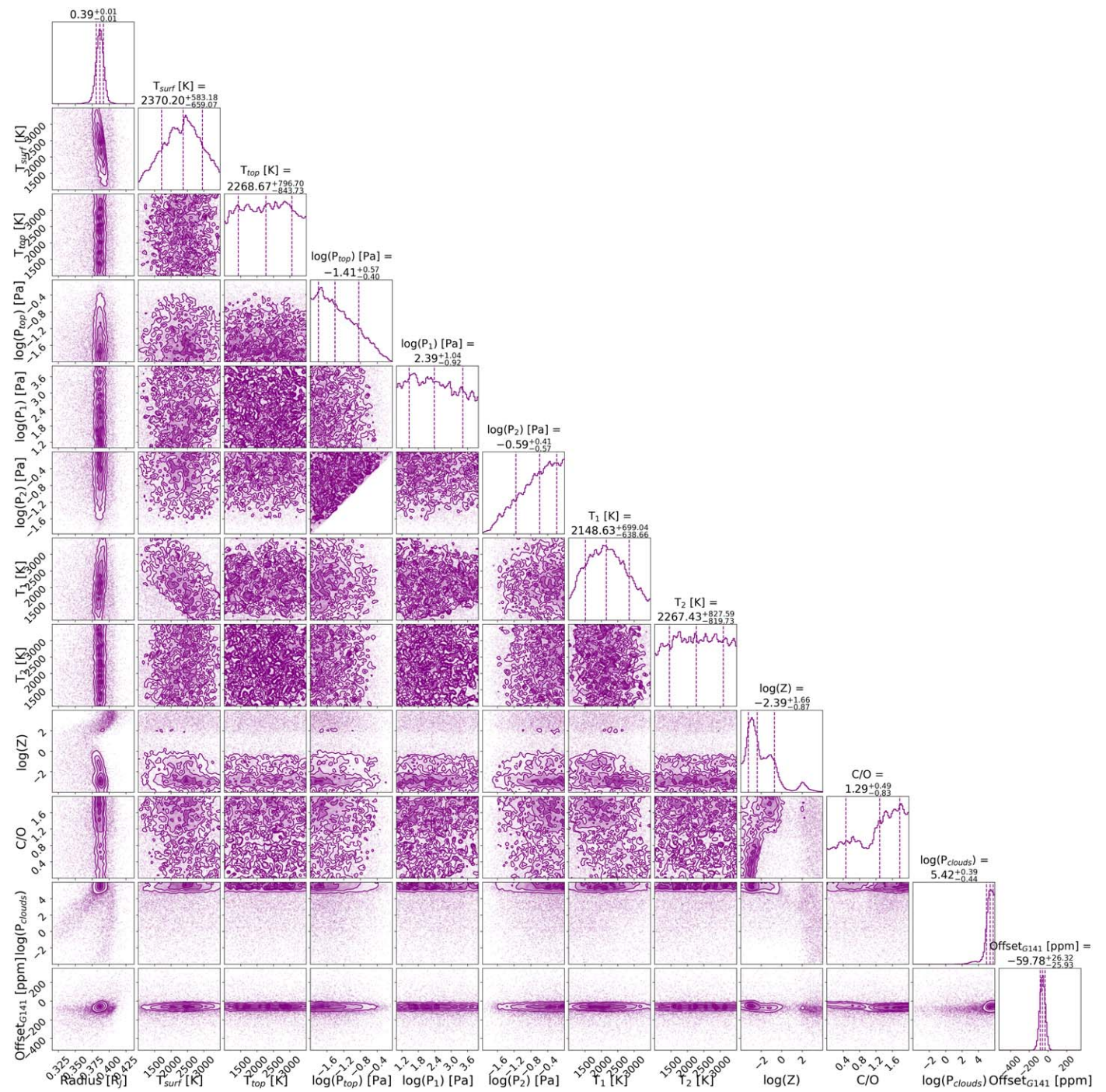


**Figure 22.** Posterior distributions for the chemical equilibrium retrieval which included an offset in the HST WFC3 G141 data. The retrieval converges to a solution which has a significant offset. However, the Bayesian evidence for this retrieval is significantly less than that of the same retrieval minus an offset parameter. The difference in the Bayesian evidence suggests an offset between the data sets is rejected at the  $3.4\sigma$  level, the same degree to which the free chemistry retrievals prefer a lack of offset.

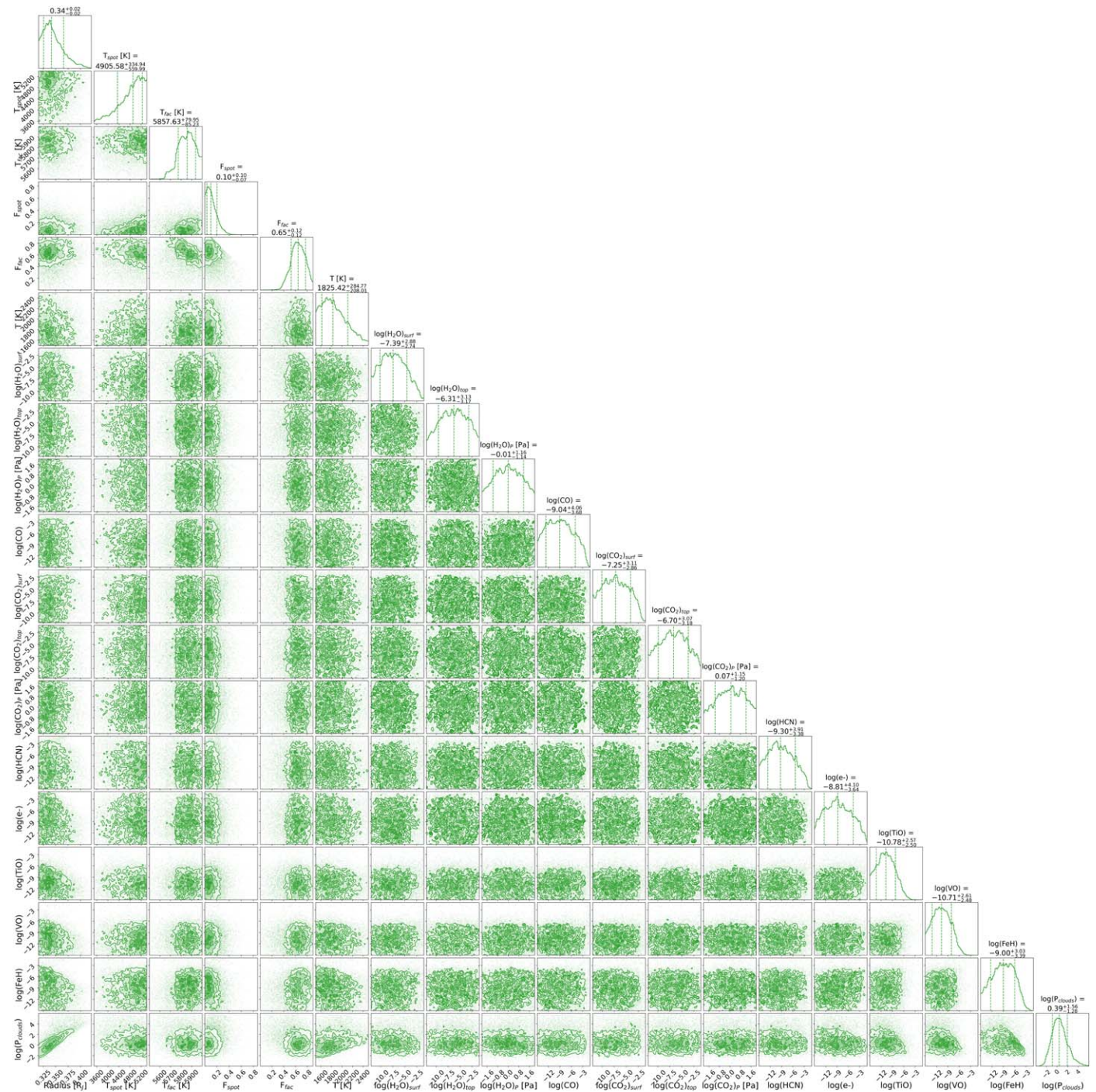


**Figure 23.** Posterior distributions for our free chemistry retrieval which accounted for spots and faculae. The retrieval prefers a solution without an atmospheric detection for LTT 9779 b and instead favors a very large, and unlikely, faculae covering fraction.

**Table 3**

The HST WFC3 G102 Spectrum Extracted in this Work and the HST WFC3 G141 Spectrum from Edwards et al. (2022)

Wavelength ( $\mu\text{m}$ )	Transit Depth (%)	Uncertainty (%)	Bandwidth ( $\mu\text{m}$ )
0.83750	0.1810	0.0077	0.0250
0.86250	0.1772	0.0087	0.0250
0.88750	0.1986	0.0071	0.0250
0.91250	0.1921	0.0066	0.0250
0.93750	0.1938	0.0060	0.0250
0.96250	0.1975	0.0060	0.0250
0.98750	0.2099	0.0054	0.0250
1.01250	0.2081	0.0051	0.0250
1.03750	0.2024	0.0051	0.0250
1.06250	0.1951	0.0041	0.0250
1.08750	0.1919	0.0056	0.0250
1.11250	0.2051	0.0066	0.0250
1.13750	0.1997	0.0051	0.0250
1.12625	0.2175	0.0064	0.0219
1.14775	0.1970	0.0060	0.0211
1.16860	0.1963	0.0087	0.0206
1.18880	0.1917	0.0071	0.0198
1.20835	0.2002	0.0062	0.0193
1.22750	0.1956	0.0065	0.0190
1.24645	0.1953	0.0071	0.0189
1.26550	0.2163	0.0056	0.0192
1.28475	0.1921	0.0062	0.0193
1.30380	0.2013	0.0060	0.0188
1.32260	0.2036	0.0073	0.0188
1.34145	0.2054	0.0076	0.0189
1.36050	0.2090	0.0071	0.0192
1.38005	0.2136	0.0073	0.0199
1.40000	0.2093	0.0065	0.0200
1.42015	0.2006	0.0062	0.0203
1.44060	0.2112	0.0063	0.0206
1.46150	0.2097	0.0058	0.0212
1.48310	0.2103	0.0052	0.0220
1.50530	0.2180	0.0070	0.0224
1.52800	0.2149	0.0051	0.0230
1.55155	0.2074	0.0060	0.0241
1.57625	0.2116	0.0063	0.0253
1.60210	0.2143	0.0060	0.0264
1.62945	0.2203	0.0061	0.0283

**Table 4**

Transit Midtimes Utilized in This Work

Transit Midtime (BJD <sub>TDB</sub> )	Uncertainty (days)	Epoch	Source
2458354.21580	0.00120	−870	TESS (K22)
2458355.00840	0.00160	−869	TESS (K22)
2458355.79800	0.00110	−868	TESS (K22)
2458357.38318	0.00099	−866	TESS (K22)
2458358.17580	0.00110	−865	TESS (K22)
2458358.96760	0.00200	−864	TESS (K22)
2458359.75890	0.00110	−863	TESS (K22)
2458360.55100	0.00130	−862	TESS (K22)

**Table 4**

(Continued)

Transit Midtime (BJD <sub>TDB</sub> )	Uncertainty (days)	Epoch	Source
2458361.34230	0.00140	−861	TESS (K22)
2458362.13651	0.00100	−860	TESS (K22)
2458362.92650	0.00130	−859	TESS (K22)
2458363.71870	0.00100	−858	TESS (K22)
2458364.51130	0.00120	−857	TESS (K22)
2458365.30484	0.00077	−856	TESS (K22)
2458366.09510	0.00100	−855	TESS (K22)
2458366.88765	0.00100	−854	TESS (K22)
2458369.26457	0.00074	−851	TESS (K22)
2458370.05550	0.00100	−850	TESS (K22)
2458370.84950	0.00180	−849	TESS (K22)
2458371.63979	0.00074	−848	TESS (K22)
2458372.43220	0.00210	−847	TESS (K22)
2458373.22520	0.00170	−846	TESS (K22)
2458374.01730	0.00130	−845	TESS (K22)
2458374.80930	0.00130	−844	TESS (K22)
2458375.60121	0.00092	−843	TESS (K22)
2458376.39385	0.00076	−842	TESS (K22)
2458377.18376	0.00077	−841	TESS (K22)
2458377.97850	0.00170	−840	TESS (K22)
2458378.76838	0.00080	−839	TESS (K22)
2458379.56140	0.00150	−838	TESS (K22)
2458380.35167	0.00099	−837	TESS (K22)
2458381.14590	0.00140	−836	TESS (K22)
2458781.13997	0.00032	−331	Spitzer (C20)
2458783.51684	0.00053	−328	Spitzer (C20)
2459088.45768	0.00090	57	TESS (K22)
2459089.25123	0.00093	58	TESS (K22)
2459090.04391	0.00078	59	TESS (K22)
2459090.83570	0.00110	60	TESS (K22)
2459091.62575	0.00087	61	TESS (K22)
2459092.41940	0.00100	62	TESS (K22)
2459093.21130	0.00120	63	TESS (K22)
2459094.00276	0.00100	64	TESS (K22)
2459094.79610	0.00074	65	TESS (K22)
2459095.58610	0.00170	66	TESS (K22)
2459096.37986	0.00079	67	TESS (K22)
2459097.16960	0.00260	68	TESS (K22)
2459097.96335	0.00095	69	TESS (K22)
2459102.71480	0.00130	75	TESS (K22)
2459103.50590	0.00100	76	TESS (K22)
2459104.29951	0.00077	77	TESS (K22)
2459105.09100	0.00100	78	TESS (K22)
2459105.88175	0.00080	79	TESS (K22)
2459106.67610	0.00150	80	TESS (K22)
2459107.46860	0.00180	81	TESS (K22)
2459108.25930	0.00084	82	TESS (K22)
2459109.05020	0.00100	83	TESS (K22)
2459109.84550	0.00120	84	TESS (K22)
2459110.63740	0.00140	85	TESS (K22)
2459111.42907	0.00086	86	TESS (K22)
2459112.22229	0.00092	87	TESS (K22)
2459377.56157	0.00018	422	HST (TW)
2459733.19839	0.00019	871	HST (TW)

**Note.** C20: Crossfield et al. (2020); K22: Kokori et al. (2023); TW: this work.

**Table 5**  
Eclipse Midtimes Utilized in This Work

Eclipse Midtime (BJD <sub>TDB</sub> )	Uncertainty (days)	Epoch	Source
2458354.61092	0.00205	−870	TESS (TW)
2458358.57127	0.00115	−865	TESS (TW)
2458360.94750	0.00123	−862	TESS (TW)
2458364.11575	0.00150	−858	TESS (TW)
2458368.86808	0.00102	−852	TESS (TW)
2458372.03640	0.00164	−848	TESS (TW)
2458375.20465	0.00234	−844	TESS (TW)
2458378.37286	0.00111	−840	TESS (TW)
2458541.53740	0.00110	−634	Spitzer (D20)
2458544.70430	0.00200	−630	Spitzer (D20)
2458550.24910	0.00260	−623	Spitzer (D20)
2458555.00240	0.00130	−617	Spitzer (D20)
2458562.13080	0.00200	−608	Spitzer (D20)
2458563.71590	0.00170	−606	Spitzer (D20)
2458569.25990	0.00280	−599	Spitzer (D20)
2458574.80220	0.00290	−592	Spitzer (D20)
2458780.73960	0.00670	−332	Spitzer (D20)
2458781.53340	0.00130	−331	Spitzer (D20)
2458783.11600	0.00350	−329	Spitzer (D20)
2458783.90490	0.00400	−328	Spitzer (D20)
2459088.85451	0.00153	57	TESS (TW)
2459092.02276	0.00118	61	TESS (TW)
2459095.19103	0.00125	65	TESS (TW)
2459098.35925	0.00155	69	TESS (TW)
2459104.69580	0.00132	77	TESS (TW)
2459107.86407	0.00136	81	TESS (TW)

**Note.** D20: Dragomir et al. (2020); TW: this work.

**Table 6**  
Best-fit Parameters from Our Linear, Decay, and Precession Model Fits to the Transit and Eclipse Midtimes and Radial Velocity Data of LTT 9779 b

Model	Parameter	Unit	Without Spitzer Transits	With Spitzer Transits
Linear	$P$	[days]	$0.79206406 \pm 0.00000014^a$	$0.79206380 \pm 0.00000014$
	$t_0$	[BJD <sub>TDB</sub> ]	$2459043.310621 \pm 0.000088^a$	$2459043.310895 \pm 0.000086$
Decay	$P$	[days]	$0.79206404 \pm 0.00000014$	$0.79206376 \pm 0.00000014$
	$t_0$	[BJD <sub>TDB</sub> ]	$2459043.31067 \pm 0.00015$	$2459043.31122 \pm 0.00014$
	$dP/dE$	[days epoch <sup>−1</sup> ]	$-2.4 \times 10^{-10} \pm 5.6 \times 10^{-10}$	$-1.71 \times 10^{-9} \pm 0.54 \times 10^{-9}$
	$dP/dt$	[ms yr <sup>−1</sup> ]	$-9 \pm 22$	$-68 \pm 21$
Precession	$P$	[days]	$0.79206409 \pm 0.00000015$	$0.79206476 \pm 0.00000023$
	$t_0$	[BJD <sub>TDB</sub> ]	$2459043.310601 \pm 0.000093$	$2459043.311163 \pm 0.000092$
	$\omega_0$	[rad]	$3.8 \pm 2.1$	$4.358 \pm 0.070$
	$d\omega/dE$	[rad epoch <sup>−1</sup> ]	$0.0030 \pm 0.0023$	$0.00313 \pm 0.00015$
	$e$		$0.00018 \pm 0.00042$	$0.00623 \pm 0.00082$

**Note.** Due to the significant  $O - C$  seen in the Spitzer transit midtimes, but not the Spitzer eclipse midtimes, we show the results for fits with and without these transit midtimes, preferring the latter as discussed in Section 3.3.

<sup>a</sup> Preferred ephemeris solution.

### ORCID iDs

Billy Edwards  <https://orcid.org/0000-0002-5494-3237>  
 Quentin Changeat  <https://orcid.org/0000-0001-6516-4493>  
 Angelos Tsiaras  <https://orcid.org/0000-0003-3840-1793>  
 Patrick Behr  <https://orcid.org/0000-0003-1369-8551>  
 Simone R. Hagey  <https://orcid.org/0000-0001-8072-0590>  
 Michael D. Himes  <https://orcid.org/0000-0002-9338-8600>  
 Sushuang Ma  <https://orcid.org/0000-0001-9010-0539>  
 Keivan G. Stassun  <https://orcid.org/0000-0002-3481-9052>  
 Alexandra Thompson  <https://orcid.org/0000-0003-4128-2270>

Aaron Boley  <https://orcid.org/0000-0002-0574-4418>  
 Kevin France  <https://orcid.org/0000-0002-1002-3674>  
 Natalia Lawson  <https://orcid.org/0000-0001-6508-5736>  
 Annabella Meech  <https://orcid.org/0000-0002-7500-7173>  
 Caprice L. Phillips  <https://orcid.org/0000-0001-5610-5328>  
 Aline A. Vidotto  <https://orcid.org/0000-0001-5371-2675>  
 Kai Hou Yip  <https://orcid.org/0000-0002-9616-1524>  
 Michelle Bieger  <https://orcid.org/0000-0001-9166-3042>  
 Amélie Gressier  <https://orcid.org/0000-0003-0854-3002>  
 Ing-Guey Jiang  <https://orcid.org/0000-0001-7359-3300>

Pietro Leonardi  <https://orcid.org/0000-0001-6026-9202>  
 Nour Skaf  <https://orcid.org/0000-0002-9372-5056>  
 Jake Taylor  <https://orcid.org/0000-0003-4844-9838>  
 Ming Yang  <https://orcid.org/0000-0002-6926-2872>  
 Derek Ward-Thompson  <https://orcid.org/0000-0003-1140-2761>

## References

- Abel, M., Frommhold, L., Li, X., & Hunt, K. L. 2011, *JPCA*, **115**, 6805  
 Abel, M., Frommhold, L., Li, X., & Hunt, K. L. 2012, *JChPh*, **136**, 044319  
 Allan, A., & Vidotto, A. A. 2019, *MNRAS*, **490**, 3760  
 Allard, F., Homeier, D., & Freytag, B. 2012, *RSPTA*, **370**, 2765  
 Allart, R., Bourrier, V., Lovis, C., et al. 2018, *Sci*, **362**, 1384  
 Al-Refaie, A. F., Changeat, Q., Venot, O., Waldmann, I. P., & Tinetti, G. 2022, *ApJ*, **932**, 123  
 Al-Refaie, A. F., Changeat, Q., Waldmann, I. P., & Tinetti, G. 2021, *ApJ*, **917**, 37  
 Anderson, D. R., Collier Cameron, A., Delrez, L., et al. 2017, *A&A*, **604**, A110  
 Anderson, R. E., Regan, M., Valenti, J., & Bergeron, E. 2014, arXiv:1402.4181  
 Anisman, L. O., Chubb, K. L., Changeat, Q., et al. 2022a, *JQSR*, **283**, 108146  
 Anisman, L. O., Chubb, K. L., Elsey, J., et al. 2022b, *JQSR*, **278**, 108013  
 Anisman, L. O., Edwards, B., Changeat, Q., et al. 2020, *AJ*, **160**, 233  
 Arcangeli, J., Désert, J.-M., Parmentier, V., et al. 2019, *A&A*, **625**, A136  
 Astropy Collaboration, Price-Whelan, A. M., Sipőcz, B. M., et al. 2018, *AJ*, **156**, 123  
 Ballerini, P., Micela, G., Lanza, A. F., & Pagano, I. 2012, *A&A*, **539**, A140  
 Barber, R. J., Strange, J. K., Hill, C., et al. 2013, *MNRAS*, **437**, 1828  
 Barclay, T., Kostov, V. B., Colón, K. D., et al. 2021, *AJ*, **162**, 300  
 Beaugé, C., & Nesvorný, D. 2013, *ApJ*, **763**, 12  
 Borucki, W. J., Koch, D., Basri, G., et al. 2010, *Sci*, **327**, 977  
 Brande, J., Crossfield, I. J. M., Kreidberg, L., et al. 2022, *AJ*, **164**, 197  
 Buchner, J., Georgakakis, A., Nandra, K., et al. 2014, *A&A*, **564**, A125  
 Carolan, S., Vidotto, A. A., Villarreal D'Angelo, C., & Hazra, G. 2021, *MNRAS*, **500**, 3382  
 Changeat, Q. 2022, *AJ*, **163**, 106  
 Changeat, Q., Al-Refaie, A. F., Edwards, B., Waldmann, I. P., & Tinetti, G. 2021, *ApJ*, **913**, 73  
 Changeat, Q., & Edwards, B. 2021, *ApJL*, **907**, L22  
 Changeat, Q., Edwards, B., Al-Refaie, A. F., et al. 2020, *AJ*, **160**, 260  
 Changeat, Q., Edwards, B., Al-Refaie, A. F., et al. 2022, arXiv:2211.00649  
 Changeat, Q., Edwards, B., Waldmann, I. P., & Tinetti, G. 2019, *ApJ*, **886**, 39  
 Collette, A. 2013, Python and HDF5 (Sebastopol, CA: O'Reilly)  
 Crossfield, I. J. M., Dragomir, D., Cowan, N. B., et al. 2020, *ApJL*, **903**, L7  
 Cubillos, P. E., & Blečić, J. 2021, *MNRAS*, **505**, 2675  
 Doyon, R., Hutchings, J. B., Beaulieu, M., et al. 2012, *Proc. SPIE*, **8442**, 84422R  
 Dragomir, D., Crossfield, I. J. M., Benneke, B., et al. 2020, *ApJL*, **903**, L6  
 Edwards, B., Anisman, L., Changeat, Q., et al. 2020a, HST Proposal, Cycle 28 16457  
 Edwards, B., Changeat, Q., Baeyens, R., et al. 2020b, *AJ*, **160**, 8  
 Edwards, B., Changeat, Q., Mori, M., et al. 2021, *AJ*, **161**, 44  
 Edwards, B., Changeat, Q., Tsiaras, A., et al. 2022, arXiv:2211.00649  
 Edwards, B., Mugnai, L., Tinetti, G., Pascale, E., & Sarkar, S. 2019, *AJ*, **157**, 242  
 Feroz, F., Hobson, M. P., & Bridges, M. 2009, *MNRAS*, **398**, 1601  
 Fisher, C., & Heng, K. 2018, *MNRAS*, **481**, 4698  
 Fletcher, L. N., Gustafsson, M., & Orton, G. S. 2018, *ApJS*, **235**, 24  
 Foreman-Mackey, D. 2016, *JOSS*, **1**, 24  
 Foreman-Mackey, D., Hogg, D. W., Lang, D., & Goodman, J. 2013, *PASP*, **125**, 306  
 France, K., Bean, J. L., Berta-Thompson, Z. K., et al. 2020, HST Proposal, Cycle 28, 16166  
 Fulton, B. J., Petigura, E. A., Blunt, S., & Sinukoff, E. 2018, *PASP*, **130**, 044504  
 Garcia, L. J., Moran, S. E., Rackham, B. V., et al. 2022, *A&A*, **665**, A19  
 Goldreich, P., & Soter, S. 1966, *Icar*, **5**, 375  
 Gordon, I., Rothman, L. S., Wilzewski, J. S., et al. 2016, AAS/DPS Meeting Abstracts, **48**, 421.13  
 Guilluy, G., Gressier, A., Wright, S., et al. 2021, *AJ*, **161**, 19  
 Guo, X., Crossfield, I. J. M., Dragomir, D., et al. 2020, *AJ*, **159**, 239  
 Hagey, S. R., Edwards, B., & Boley, A. C. 2022, *AJ*, **164**, 220  
 Heyl, J. S., & Gladman, B. J. 2007, *MNRAS*, **377**, 1511  
 Himes, M. D., & Harrington, J. 2022, *ApJ*, **931**, 86  
 Hunter, J. D. 2007, *CSE*, **9**, 90  
 Jacobs, B., Désert, J. M., Pino, L., et al. 2022, *A&A*, **668**, L1  
 Jenkins, J. S., Díaz, M. R., Kurtovic, N. T., et al. 2020, *NatAs*, **4**, 1148  
 John, T. L. 1988, *A&A*, **193**, 189  
 Kokori, A., Tsiaras, A., Edwards, B., et al. 2021, *ExA*, **53**, 547  
 Kokori, A., Tsiaras, A., Edwards, B., et al. 2023, *ApJS*, **265**, 4  
 Kokori, A., Tsiaras, A., Edwards, B., et al. 2022, *ApJS*, **258**, 40  
 Kramm, U., Nettelmann, N., Redmer, R., & Stevenson, D. J. 2011, *A&A*, **528**, A18  
 Kreidberg, L., Bean, J. L., Désert, J.-M., et al. 2014, *Natur*, **505**, 69  
 Kreidberg, L., Line, M. R., Parmentier, V., et al. 2018, *AJ*, **156**, 17  
 Levrard, B., Winisdoerffer, C., & Chabrier, G. 2009, *ApJ*, **692**, L9  
 Li, G., Gordon, I. E., Rothman, L. S., et al. 2015, *ApJS*, **216**, 15  
 Libby-Roberts, J. E., Berta-Thompson, Z. K., Diamond-Lowe, H., et al. 2022, *AJ*, **164**, 59  
 Line, M. R., Stevenson, K. B., Bean, J., et al. 2016, *AJ*, **152**, 203  
 Linsky, J. L., Fontenla, J., & France, K. 2014, *ApJ*, **780**, 61  
 Lopez, E. D. 2017, *MNRAS*, **472**, 245  
 Lundkvist, M. S., Kjeldsen, H., Albrecht, S., et al. 2016, *NatCo*, **7**, 11201  
 Luque, R., Casasayas-Barris, N., Parviainen, H., et al. 2020, *A&A*, **642**, A50  
 Maciejewski, G., Dimitrov, D., Fernández, M., et al. 2016, *A&A*, **588**, L6  
 Mansfield, M., Bean, J. L., Oklopčić, A., et al. 2018, *ApJL*, **868**, L34  
 Mansfield, M., Line, M. R., Bean, J. L., et al. 2021, *NatAs*, **5**, 1224  
 Matsumura, S., Peale, S. J., & Rasio, F. A. 2010, *ApJ*, **725**, 1995  
 Mazeh, T., Holczer, T., & Faigler, S. 2016, *A&A*, **589**, A75  
 McCullough, P., & MacKenty, J. 2012, Space Telescope WFC Instrument Science Report, STScI  
 McCullough, P. R., Crouzet, N., Deming, D., & Madhusudhan, N. 2014, *ApJ*, **791**, 55  
 McGruder, C. D., López-Morales, M., Kirk, J., et al. 2022, *AJ*, **164**, 134  
 McKemmish, L. K., Masseron, T., Hoeijmakers, H. J., et al. 2019, *MNRAS*, **488**, 2836  
 McKemmish, L. K., Yurchenko, S. N., & Tennyson, J. 2016, *MNRAS*, **463**, 771  
 McKinney, W. 2011, Python for High Performance and Scientific Computing 14  
 Morello, G., Claret, A., Martin-Lagarde, M., et al. 2020, *AJ*, **159**, 75  
 Murgas, F., Chen, G., Nortmann, L., Palle, E., & Nowak, G. 2020, *A&A*, **641**, A158  
 Nortmann, L., Pallé, E., Salz, M., et al. 2018, *Sci*, **362**, 1388  
 Oklopčić, A. 2019, *ApJ*, **881**, 133  
 Oklopčić, A., & Hirata, C. M. 2018, *ApJL*, **855**, L11  
 Oliphant, T. E. 2006, A Guide to NumPy, Vol. 1 (USA: Trelgol Publishing)  
 Patra, K. C., Winn, J. N., Holman, M. J., et al. 2017, *AJ*, **154**, 4  
 Patra, K. C., Winn, J. N., Holman, M. J., Gillon, M., & Burdanov, A. 2020, *AJ*, **159**, 150  
 Pearson, K. A. 2019, *AJ*, **158**, 243  
 Peek, J., Desai, V., White, R. L., et al. 2019, *BAAS*, **51**, 105  
 Penev, K., Bouma, L. G., Winn, J. N., & Hartman, J. D. 2018, *AJ*, **155**, 165  
 Pluriel, W., Whiteford, N., Edwards, B., et al. 2020, *AJ*, **160**, 112  
 Polyansky, O. L., Kyuberis, A. A., Zobov, N. F., et al. 2018, *MNRAS*, **480**, 2597  
 Rackham, B. V., Apai, D., & Giampapa, M. S. 2018, *ApJ*, **853**, 122  
 Radica, M., Allart, R., Cowan, N. B., et al. 2022, HST Proposal, Cycle 29 16915  
 Ragozzine, D., & Wolf, A. S. 2009, *ApJ*, **698**, 1778  
 Ricker, G. R., Winn, J. N., Vanderspek, R., et al. 2014, *Proc. SPIE*, **9143**, 914320  
 Robbins-Blanch, N., Kataria, T., Batalha, N. E., & Adams, D. J. 2022, *ApJ*, **930**, 93  
 Rocchetto, M., Waldmann, I. P., Venot, O., Lagage, P. O., & Tinetti, G. 2016, *ApJ*, **833**, 120  
 Rothman, L., Gordon, I., Barber, R., et al. 2010, *JQSR*, **111**, 2139  
 Rothman, L. S., & Gordon, I. E. 2014, in 13th International HITRAN Conf. (Cambridge, MA: Harvard)  
 Roudier, G. M., Swain, M. R., Gudipati, M. S., et al. 2021, *AJ*, **162**, 37  
 Saba, A., Tsiaras, A., Morvan, M., et al. 2022, *AJ*, **164**, 2  
 Sing, D. K., Fortney, J. J., Nikolov, N., et al. 2016, *Natur*, **529**, 59  
 Skaf, N., Bieger, M. F., Edwards, B., et al. 2020, *AJ*, **160**, 109  
 Smith, J. C., Stumpe, M. C., Van Cleve, J. E., et al. 2012, *PASP*, **124**, 1000  
 Spake, J. J., Sing, D. K., Evans, T. M., et al. 2018, *Natur*, **557**, 68  
 Stassun, K. G., Collins, K. A., & Gaudi, B. S. 2017, *AJ*, **153**, 136  
 Stassun, K. G., Corsaro, E., Pepper, J. A., & Gaudi, B. S. 2018, *AJ*, **155**, 22  
 Stassun, K. G., & Torres, G. 2016, *AJ*, **152**, 180  
 Stassun, K. G., & Torres, G. 2021, *ApJL*, **907**, L33  
 Stevenson, K. B., Désert, J.-M., Line, M. R., et al. 2014, *Sci*, **346**, 838  
 Stevenson, K. B., Line, M. R., Bean, J. L., et al. 2017, *AJ*, **153**, 68

- Stumpe, M. C., Smith, J. C., Catanzarite, J. H., et al. 2014, *PASP*, **126**, 100
- Stumpe, M. C., Smith, J. C., Van Cleve, J. E., et al. 2012, *PASP*, **124**, 985
- Swain, M. R., Vasisht, G., & Tinetti, G. 2008, arXiv:0802.1030
- Szabó, G. M., & Kiss, L. L. 2011, *ApJL*, **727**, L44
- Tennyson, J., Yurchenko, S. N., Al-Refaie, A. F., et al. 2016, *JMoSp*, **327**, 73
- Thompson, A., Biagini, A., Cracchiolo, G., et al. 2023, arXiv:2302.04574
- Tinetti, G., Drossart, P., Eccleston, P., et al. 2018, *ExA*, **46**, 135
- Tinetti, G., Eccleston, P., Haswell, C., et al. 2021, arXiv:2104.04824
- Tinetti, G., Vidal-Madjar, A., Liang, M.-C., et al. 2007, *Natur*, **448**, 169
- Torres, G., Andersen, J., & Giménez, A. 2010, *A&ARv*, **18**, 67
- Tsiaras, A., Rocchetto, M., Waldmann, I. P., et al. 2016a, *ApJ*, **820**, 99
- Tsiaras, A., Waldmann, I., Rocchetto, M., et al. 2016b, Pylightcurve, Astrophysics Source Code Library, ascl:1612.018
- Tsiaras, A., Waldmann, I. P., Rocchetto, M., et al. 2016c, *ApJ*, **832**, 202
- Tsiaras, A., Waldmann, I. P., Zingales, T., et al. 2018, *AJ*, **155**, 156
- Turner, J. D., Ridden-Harper, A., & Jayawardhana, R. 2020, *AJ*, **161**, 72
- Virtanen, P., Gommers, R., Oliphant, T. E., et al. 2020, *NatMe*, **17**, 261
- Vissapragada, S., Knutson, H. A., Greklek-McKeon, M., et al. 2022, *AJ*, **164**, 234
- Wende, S., Reiners, A., Seifahrt, A., & Bernath, P. F. 2010, *A&A*, **523**, A58
- Wilson, J., Gibson, N. P., Nikolov, N., et al. 2020, *MNRAS*, **497**, 5155
- Woitke, P., Helling, C., Hunter, G. H., et al. 2018, *A&A*, **614**, A1
- Wong, I., Shporer, A., Vissapragada, S., et al. 2022, *AJ*, **163**, 175
- Woods, T. N., Chamberlin, P. C., Harder, J. W., et al. 2009, *GeoRL*, **36**, L01101
- Yan, F., Espinoza, N., Molaverdikhani, K., et al. 2020, *A&A*, **642**, A98
- Yee, S. W., Winn, J. N., Knutson, H. A., et al. 2019, *ApJL*, **888**, L5
- Yip, K. H., Changeat, Q., Edwards, B., et al. 2021, *AJ*, **161**, 4
- Youngblood, A., Pineda, J. S., Ayres, T., et al. 2022, *ApJ*, **926**, 129
- Zhang, M., Knutson, H. A., Dai, F., et al. 2023, *AJ*, **165**, 62